Article

Developmental Cell

Identification of long-lived proteins in the mitochondria reveals increased stability of the electron transport chain

Graphical abstract

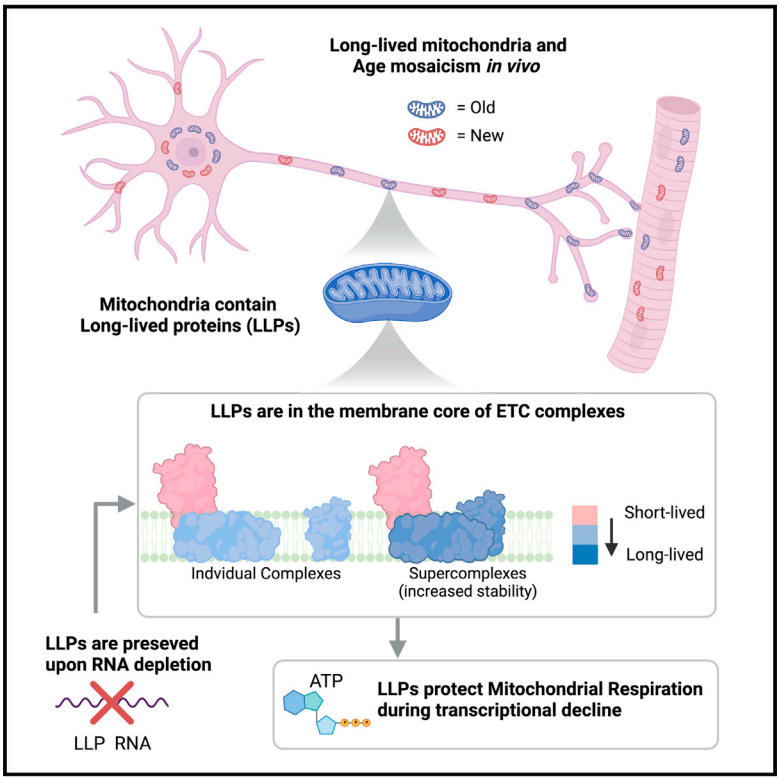

Highlights

- Mitochondria in the mouse brain are long lived and show considerable age mosaicism
- Mitochondria contain many LLPs as part of protein complexes
- LLPs in the electron transport chain show increased stability within supercomplexes
- Longevity of LLP COX7C preserves oxphos function despite transcriptional decline

Authors

Shefali Krishna, Rafael Arrojo e Drigo, Juliana S. Capitanio, Ranjan Ramachandra, Mark Ellisman, Martin W. Hetzer

Correspondence

hetzer@salk.edu

In brief

Krishna et al. discover that mitochondria in neurons and muscle fibers exhibit slow turnover and contain many long-lived proteins that can be part of large protein complexes. The longevity of these proteins in the electron transport chain can maintain oxphos complex assembly and mitochondrial function despite their transcriptional decline.

Krishna et al., 2021, Developmental Cell *56*, 1–14
November 8, 2021
https://doi.org/10.1016/j.devcel.2021.10.008

CellPress

Developmental Cell

CellPress

Article

Identification of long-lived proteins in the mitochondria reveals increased stability of the electron transport chain

Shefali Krishna,[1] Rafael Arrojo e Drigo,[1,2,4] Juliana S. Capitanio,[1] Ranjan Ramachandra,[2,3] Mark Ellisman,[2,3] and Martin W. Hetzer[1,5,*]

[1]Molecular and Cell Biology Laboratory (MCBL), Salk Institute for Biological Studies, La Jolla, CA 92037, USA
[2]National Center for Microscopy and Imaging Research (NCMIR), University of California, San Diego School of Medicine (UCSD), La Jolla, CA 92093, USA
[3]Department of Neurosciences, University of California, San Diego School of Medicine (UCSD), La Jolla, CA 92093, USA
[4]Present address: Molecular Physiology and Biophysics Department, Vanderbilt University, Nashville, TN 37232, USA
[5]Lead contact
*Correspondence: hetzer@salk.edu
https://doi.org/10.1016/j.devcel.2021.10.008

SUMMARY

In order to combat molecular damage, most cellular proteins undergo rapid turnover. We have previously identified large nuclear protein assemblies that can persist for years in post-mitotic tissues and are subject to age-related decline. Here, we report that mitochondria can be long lived in the mouse brain and reveal that specific mitochondrial proteins have half-lives longer than the average proteome. These mitochondrial long-lived proteins (mitoLLPs) are core components of the electron transport chain (ETC) and display increased longevity in respiratory supercomplexes. We find that COX7C, a mitoLLP that forms a stable contact site between complexes I and IV, is required for complex IV and supercomplex assembly. Remarkably, even upon depletion of COX7C transcripts, ETC function is maintained for days, effectively uncoupling mitochondrial function from ongoing transcription of its mitoLLPs. Our results suggest that modulating protein longevity within the ETC is critical for mitochondrial proteome maintenance and the robustness of mitochondrial function.

INTRODUCTION

Protein homeostasis is critical for maintaining cell function and organismal health. As proteins age, they accumulate molecular damage that causes them to dysfunction and aggregate (Hipp et al., 2019). For example, mitochondrial protein aggregation has been observed during aging in *C. elegans* (David et al., 2010). Also, the mitochondrial matrix proteases Lon and ClpXP that degrade misfolded proteins show reduced activity with age in humans (Bezawork-Geleta et al., 2015). This loss of proteostasis could contribute to the age-related decline in mitochondrial function and respiratory capacity (López-Otín et al., 2013), particularly since the mitochondrial proteome is vulnerable to damage due to the high levels of reactive oxygen species (ROS) generated from the ETC (Moehle et al., 2019). Damaged mitochondrial proteins can lead to ETC dysfunction and further ROS production that would promote mtDNA mutations and compromise organelle function (Moehle et al., 2019). To counteract this, mitochondria have evolved several protein quality control mechanisms. These include resident mitochondrial chaperones and AAA-proteases, cytosolic ubiquitin/proteasomal machinery, mitochondrial unfolded protein response, and lysosomal degradation of mitochondrial-derived vesicles (Picca et al., 2020; Shpilka and Haynes, 2018; Song et al., 2021). Finally, clearance of whole mitochondria or specific regions can occur through mitophagy that is in part regulated by PINK1 and Parkin, both of which are highly implicated in Parkinson's disease (Palikaras et al., 2018).

Another critical protein quality control mechanism is protein turnover or recycling. To combat the accumulation of damaged proteins, the majority of the cellular proteome turns over rapidly, a process that is crucial for post-mitotic cells such as neurons and muscle fibers as they are unable to dilute the deleterious proteins via cell division (Toyama and Hetzer, 2013). Interestingly, we have recently identified proteins in the rat brain that are extremely long lived and can persist for months or even years (Savas et al., 2012; Toyama et al., 2013). These long-lived proteins (LLPs) are found primarily in the nucleus or the plasma membrane/extracellular matrix. Many of the nuclear LLPs are components of large protein complexes, such as histones H3.1/H4 in the nucleosome, lamin-B1/B2 in the nuclear lamina, and nucleoporins (nups) of the nuclear pore complex (NPC), which is required for nuclear membrane transport (Toyama et al., 2013). By imaging cortical neurons using correlated

Please cite this article in press as: Krishna et al., Identification of long-lived proteins in the mitochondria reveals increased stability of the electron transport chain, Developmental Cell (2021), https://doi.org/10.1016/j.devcel.2021.10.008

multi-isotope imaging mass spectroscopy and scanning electron microscopy (MIMS-EM), we have also established that NPCs are long-lived structures *in vivo* (Toyama et al., 2019). Interestingly, we have found that not all NPCs are long lived and that protein turnover within the NPC itself is also heterogeneous, with peripheral nups being short lived and scaffold nups being long lived (Toyama et al., 2013). This molecular age mosaicism raises key questions about the role of protein longevity in macromolecular complexes. LLPs could be critical for maintaining a scaffold for the structural and functional integrity of complexes. They may also be prone to damage due to their long-lived nature, leading to impaired function with age. Indeed, aged neurons show more damage in long-lived nups and have impaired nuclear transport that results in accumulation of cytosolic proteins in the nucleus (D'Angelo et al., 2009). Such intranuclear aggregates have also been seen in neurons from patients with neurodegenerative disease, providing an unexpected link between LLPs and age-related disorders (D'Angelo et al., 2009).

While extreme protein longevity has been seen in the nucleus—an organelle that is not replaced in post-mitotic cells, the turnover of mitochondria is poorly understood. Although our original studies primarily detected nuclear LLPs (Toyama et al., 2013), there have been reports that certain mitochondrial proteins can have half-lives of one month in the mouse brain (Fornasiero et al., 2018; Price et al., 2010). Some of these proteins were also components of the ETC. Interestingly, it was recently shown that the ETC exists as individual complexes (ICs) as well as higher-order quaternary structures called "supercomplexes" (SCs) (Gu et al., 2016; Letts et al., 2016). However, there are no reports of protein half-lives in the SCs compared with the ICs, as the previous studies used tissue homogenates without separating the different complexes (Fornasiero et al., 2018; Price et al., 2010). Also, the precise role of SCs in the ETC is unclear, with some reports suggesting that they could increase the stability of complex I (CI) (Letts and Sazanov, 2017). Hence, the identification of LLPs and characterization of their role in in the ETC is critical to understanding mitochondrial protein homeostasis.

In this study, we find that neurons and muscle fibers have mitochondria that are long lived and can persist up to 6 months *in vivo*. Moreover, we find considerable age mosaicism between different mitochondria, a phenomenon that we also demonstrate in neurons *in vitro*. We further determine *in vitro* that mitochondria turn over slower compared with the cellular proteome, with many proteins exhibiting longer than average lifespans. These mitoLLPs are core components of the ETC, specifically the membrane arm of CI and complex III (CIII). Remarkably, we find that these LLPs display increased stability in the SCs compared with ICs. One of the critical interactions between CI and complex IV (CIV) is stabilized by COX7C, a mitoLLP that shows an age-dependent decline in transcription (Su et al., 2015). We recapitulate this decline and find that despite depletion of COX7C transcripts, the protein still persists and is able to protect myotubes from loss-of-function defects in CIV and SC assembly. These data show that mitoLLPs could potentially be required for maintaining stability and function of the ETC in times of transcriptional decline during cellular stress or aging.

RESULTS

Discovery of long-lived mitochondria in post-mitotic tissues of 6-month-old mice

While there are thousands of mitochondria in each cell, and even more in highly metabolic tissues, how long individual mitochondria can persist is unknown. To study the lifespan of mitochondria in post-mitotic tissues, we performed ^{15}N-SILAM labeling of mice coupled with MIMS-EM, which can help visualize protein, organelle, and cell turnover *in vivo* (Arrojo et al., 2019). Briefly, female mice were fed an ^{15}N diet, followed by a chase with ^{14}N until 6 months of age, when mitochondria-dense tissues such as brain and skeletal muscle were harvested and imaged (see STAR Methods). MIMS images represent the ^{15}N-to-^{14}N ratio, and since ^{15}N is lost during cell and/or protein turnover, the ^{15}N/^{14}N is a reporter of "old" versus "new" for cells and protein complexes (Toyama et al., 2019). The MIMS images were colorized based on the fold increase over the natural ratio (NR) of ^{15}N/^{14}N at 37 × 10^{-4} (Figure S1A). As seen before with post-mitotic cells (Arrojo et al., 2019), the nuclei of cerebellar granule cell neurons show a ^{15}N/^{14}N > 50× above the NR (Figures 1A and 1B, black arrow). In contrast, structures such as blood vessel lumens in the cerebellum or intercostal muscle (ICM) show minimal ^{15}N/^{14}N signal (Figures 1C, 1F, and 1G). As this was the lowest signal seen, we used a ^{15}N/^{14}N of 55 × 10^{-4} (1.5× NR) as our background. These data support our previous observations that most ^{15}N signal is retained in the nucleus of non-dividing cells, which includes DNA and nuclear LLPs (Toyama et al., 2013).

Remarkably, we found that the majority of mitochondria in cerebellar neurons show an increased ^{15}N/^{14}N signal in the range of 2-to-3× NR, with many clusters that are as high as 3-to-7× NR (Figures 1A and 1B, yellow rectangle). Indeed, these clusters show signals similar to the myelin sheath itself, which is known to contain LLPs and is consistently labeled in MIMS-EM studies (Figures 1A and 1B, red arrows) (Arrojo et al., 2019; Toyama et al., 2013). Interestingly, these clusters of old mitochondria specifically reside in the axonal terminals and synaptic boutons of mossy fiber neurons (Figure 1B, inset, black arrow). These axonal processes form large pre-synaptic terminals with the post-synaptic processes of granule cell dendrites, which themselves primarily contain mitochondria with lower signal (Figure 1B, inset, yellow arrow). These data demonstrate considerable heterogeneity in mitochondrial age in the same tissue. Quantification of the ^{15}N/^{14}N of individual mitochondria shows that granule cell dendritic mitochondria have "lower" signal at ~1.9× NR while the axonal mitochondria have "higher" signal at 4× NR (Figure 1C). These results reveal ^{15}N retention in neuronal mitochondria, signifying the presence of mitochondrial components that are long lived and have limited turnover in 6-month-old mice. Given that mitochondria have always been considered a dynamic organelle undergoing constant fission/fusion, the presence of these clusters of long-lived mitochondria is an important finding. Moreover, the "higher" signal axonal population shows a significant level of variability in the ^{15}N/^{14}N signal (Figure 1C), suggesting that mitochondria in the same cell can also have different lifespans. These data indicate age mosaicism within mitochondria, similar to what has been observed at the cellular and protein level in the brain, liver, and

Please cite this article in press as: Krishna et al., Identification of long-lived proteins in the mitochondria reveals increased stability of the electron transport chain, Developmental Cell (2021), https://doi.org/10.1016/j.devcel.2021.10.008

CellPress

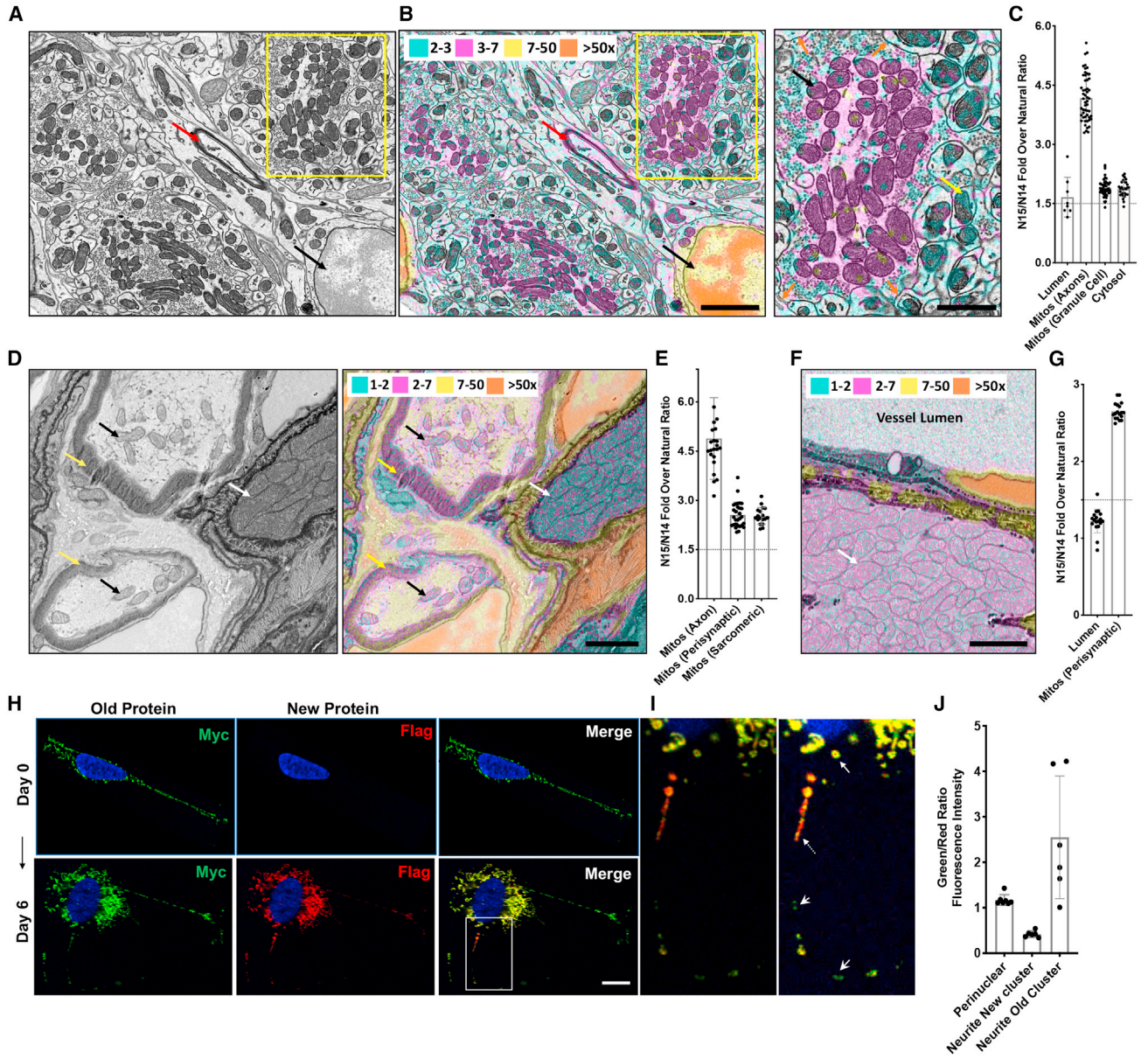

Figure 1. Discovery of long-lived mitochondria in post-mitotic tissues of 6-month-old mice

(A and B) SEM image (A) and MIMS (B) overlay of cerebellar neurons from a 6-month chase mouse. Nucleus of a granule cell neuron (black arrow), myelin sheath (red arrows), and mitochondria (inset, B-right panel) are indicated. Inset shows mitochondria in mossy fibers axons containing "higher" (black arrow) and granule cell dendrites containing "lower" (yellow arrow) signal. Orange arrows show the boundary between mossy fiber axons and granule cell dendrites. $^{15}N/^{14}N$ signal thresholds over the natural ratio (NR) of 37×10^{-4}: 2–3× (cyan), 3–7× (magenta), 7–50× (yellow), >50× (vermillion).

(C) Dot plot overlaid with a bar graph shows the $^{15}N/^{14}N$ fold over the NR for blood vessel lumen (lumen, n = 8), mitochondria from mossy fiber axons (Mitos-Axons, n = 53), mitochondria from granule cell dendrites (Mitos-Granule cells, n = 50), and the cytosol (cytosol, n = 29). For the mitos plots, each dot represents the $^{15}N/^{14}N$ fold ratio for individual mitochondria whereas for the lumen and cytosol, each dot represents different regions of those structures.

(D) SEM image (left) and MIMS overlay (right) of myelinated axons near a neuromuscular junction in intercostal muscle from a 6-month chase mouse. Individual mitochondria in two myelinated axons (mitochondria, black arrows; myelin, yellow arrows), and perisynaptic mitochondria aggregates in a muscle fiber (white arrow) are indicated. $^{15}N/^{14}N$ thresholds: 1–2× (cyan), 2–7× (magenta), 7–50× (yellow), >50× (vermillion).

(E) Dot plot overlaid with a bar graph shows the $^{15}N/^{14}N$ fold over NR for mitochondria from axons (n = 23) and perisynaptic aggregates (n = 28), and sarcomeric mitochondria in the muscle fiber (n = 18).

(F) MIMS overlay of intercostal muscle fiber containing mitochondria (white arrow) next to a vessel lumen (indicated).

(G) Graph shows the $^{15}N/^{14}N$ fold over NR for regions of the blood vessel lumen (lumen, n = 18) and mitochondria (Mitos, n = 18).

(H) Turnover of ATP5C1 in SHSY-5Y neurons as measured by RITE. Images show green Myc tag (old protein, left panel) and red FLAG tag (new protein, middle panel) at day 0 (top panel) and day 6 in (bottom panel). Merge is shown in right panel.

(legend continued on next page)

Please cite this article in press as: Krishna et al., Identification of long-lived proteins in the mitochondria reveals increased stability of the electron transport chain, Developmental Cell (2021), https://doi.org/10.1016/j.devcel.2021.10.008

pancreas (Toyama et al., 2013). We next looked at myelinated axons near a neuromuscular junction (NMJ) in the ICM as they have specialized mitochondria in different regions such as the neuronal axoplasm, the terminal boutons of the motor synapse, and the non-sarcomeric and the sarcomeric regions of the muscle fiber (Figure S1B). The mitochondria in myelinated axons have high levels of $^{15}N/^{14}N$, comparable with the signal from the myelin sheath (Figures 1D and 1E) as well as the cerebellar mitochondria. We also detect increased $^{15}N/^{14}N$ in perisynaptic mitochondria aggregates at the periphery and sarcomeric mitochondria interspersed within the muscle fibers (Figures 1D, 1E, S1B, and S1C). The axonal mitochondria contain more ^{15}N, indicating that they are older than mitochondria in the muscle fibers. We also observe increased $^{15}N/^{14}N$ in mitochondria specifically in ICM muscle fibers that are not near an NMJ or neurons (Figures 1F and 1G), and in perisynaptic as well as the sarcomeric mitochondria in the fibers (Figures S1D and S1E). These data show that there are mitochondrial components that are long lived and have limited turnover in neurons and muscle fibers in 6-month-old mice, with the former having older mitochondria, as well as more heterogeneity.

The ^{15}N signal in the long-lived mitochondria *in vivo* could be from mitochondrial proteins or mtDNA. To determine specifically if mitochondrial proteins display longevity and mosaicism, we looked at protein turnover of ATP synthase subunit ATP5C1 in cultured SHSY-5Y neurons. We used a previously published technique called recombinant-induced tag exchange (RITE), where a protein expresses a Myc tag, which upon Cre-recombination gets replaced by a FLAG tag, facilitating the imaging of old (Myc) and new (FLAG) protein simultaneously (Toyama et al., 2019). This previous study showed that while nuclear LLPs turn over rapidly within 2 days in dividing cells, they persist for 1–2 weeks in post-mitotic cells *in vitro* (Toyama et al., 2019). We find that at day 0 all the ATP5C1 protein is Myc tagged (Figure 1H), and the old protein persists by day 6, despite the production of new protein (Figures 1H and S1F). Importantly, we find in the merge image that the mitochondria have differing green and red signals (Figures 1H, inset, 1I). The perinuclear mitochondria have similar green to red signal (~1), whereas the neurites have separate clusters of red and green signal indicating new and old mitochondria, respectively (Figures 1I and 1J). As seen *in vivo*, the old cluster shows considerable variability in the old/new signal. These data suggest that mitochondrial age mosaicism and heterogeneity can occur within a cell, among different cell types and tissues within the same animal, as well as in human neurons *in vitro*.

Identification of LLPs in neuronal and myotube mitochondria

Given the longevity of mitochondria and ETC proteins in post-mitotic tissues, we wanted to conduct an unbiased and comprehensive analysis of mitochondrial proteome turnover *in vitro* to determine if mitochondria contain LLPs. We use stable isotope amino acid labeling (SILAC) in human embryonic stem cells (ESH9 cells) differentiated into neurons and C2C12 myoblasts differentiated into myotubes (Figure 2A). We find that the heavy label in the whole-cell proteome went up to 60% in neurons and 80% in myotubes by day 8 (Figures S2A and S2B), indicating that while majority proteins incorporate the heavy label during the time course, neurons on average turn over slower than myotubes. Upon calculating the percentages of old protein and half-lives (see STAR Methods, Table S1), we find that the whole-cell, endoplasmic reticulum (ER), lysosomal, and cytosolic proteins in the neurons turn over rapidly with a median half-life of ~4–5 days (Figures 2B and S2C). Notably, the nuclear proteins showed a slower turnover rate due to long-lived histones, the removal of which brings nuclear turnover down to the whole-cell level (Figure S2C). Consistent with this, the median half-life of the nucleus is similar to the whole cell (Figure 2B). Remarkably, mitochondrial proteins show slower turnover than all the other organelles with a half-life of 7 days in neurons (Figures 2B and S2C). We see similar results in myotubes, with the whole-cell, nucleus, ER, cytosol, and lysosomal half-lives at ~3.5 days, whereas mitochondrial proteins are at 5.5 days (Figures 2C and S2D). These data suggest that neuronal and myotube mitochondrial proteins are indeed significantly more long lived than those residing in other organelles. Intriguingly, within the mitochondria, the outer mitochondrial membrane (OMM) proteins show similar turnover to the whole cell, whereas matrix, intermembrane space (IMS), and inner mitochondrial membrane (IMM), particularly ETC proteins, are longer lived in both neurons and myotubes (Figures S2E–S2H). This difference could be due to the OMM being recycled by cytosolic degradative pathways, while the inner compartments are dependent on mitochondrial degradative mechanisms (Vazquez-Calvo et al., 2020). Surprisingly, nucleoid proteins in neurons exhibit extremely slow turnover with half-lives up to 16 days, which was not seen in myotubes (Figures S2E, S2F, and S2H), suggesting perhaps a specialized role for these proteins in neurons.

To validate that we could indeed identify LLPs, we analyzed turnover of a known nuclear LLP histone H4. In neurons, histone H4 had 90% old protein at day 8, with a half-life of 79 days, suggesting minimal turnover (Figures 2D and 2F). The average whole-cell fraction in neurons has ~50% old protein remaining at day 8, with a standard deviation (SD) spread of ~20% (Figure 2D). While many mitochondrial proteins lie within this spread, we identified a class of mitochondrial proteins that has about 75% old protein at day 8, with half-lives ranging from 10–15 days (Figures 2D and 2F). We term this class as "mitochondrial LLPs" or "mitoLLPs" (see STAR Methods), and it contains many integral mitochondrial proteins such as CIII subunit Uqcrb, chaperone Hsp60, and nucleoid protein SSBP1 (Figures 2D and 2F). We observe similar results in myotubes, albeit with faster turnover and shorter half-lives. Histone H4 has a half-life of

(I) An inset from the merge at lower (left image) and higher fluorescent intensity (right image) shows green and red signal in mitochondria that are peri-nuclear (white arrow) or in neurites with old (white arrowhead) and new (white dashed arrow) clusters indicated.

(J) Graph shows the green/red fluorescence intensity over background for the mitochondria shown in the inset (perinuclear, n = 7; neurites new cluster, n = 6; neurites old cluster, n = 6).

For all MIMS-EM graphs, a dotted line is drawn at the background $^{15}N/^{14}N$ of 1.5× NR and error bars indicate SD. Scale bars, 5 μm (B); 2.5 μm (B, inset, D, F); and 10 μm (H).

Please cite this article in press as: Krishna et al., Identification of long-lived proteins in the mitochondria reveals increased stability of the electron transport chain, Developmental Cell (2021), https://doi.org/10.1016/j.devcel.2021.10.008

CellPress

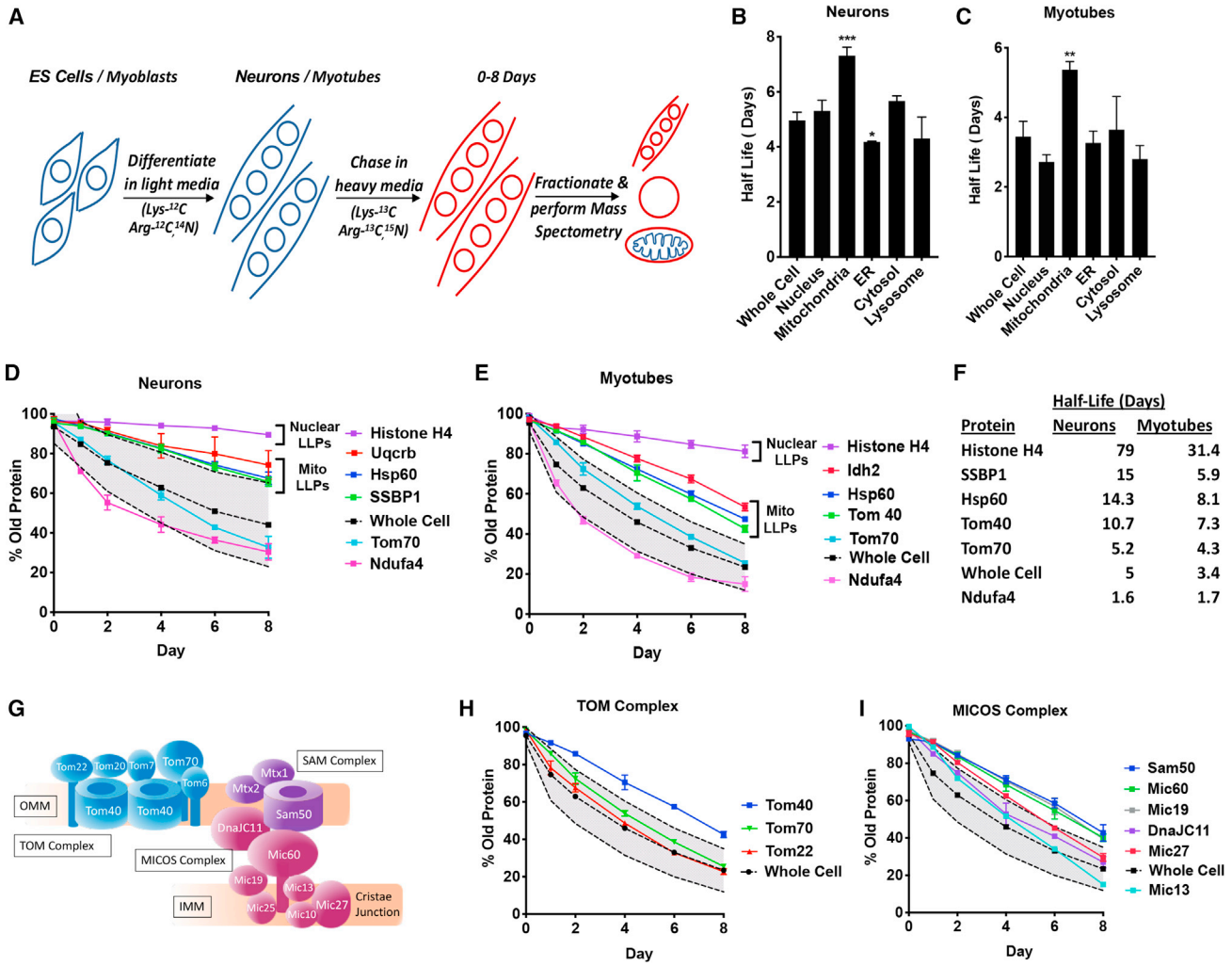

Figure 2. Identification of LLPs in neuronal and myotube mitochondria using heavy isotope labeling

(A) Schematic of the SILAC: human embryonic stem (ES) cells or C2C12 mouse myoblasts were differentiated into neurons or myotubes in light media and then switched to heavy media for 0–8 days. Whole-cell, nuclear, and mitochondrial fractions were subject to mass spectrometry. Diagram specifically shows myotubes.

(B) Graph shows median half-lives for whole cell, nucleus, mitochondria, ER, cytosol, and lysosome in neurons.

(C) Graph shows median half-lives for whole cell, ER, cytosol, and lysosome (from whole-cell fraction), nucleus (from the nuclear fraction), and mitochondria (from the mitochondrial fraction) in myotubes.

(D) Graph shows %old protein for day 0–8 for histone H4 and mitochondrial proteins Uqcrb, Hsp60, SSBP1, Tom70, and Ndufa4 in neurons. Nuclear and MitoLLPs are indicated.

(E) Graph shows %old protein for day 0–8 for the histone H4 (nuclear fraction) and mitochondrial proteins Idh2, Hsp60, Tom40, Tom70, and Ndufa4 (mitochondrial fraction) in myotubes. Nuclear and MitoLLPs are indicated.

(F) Table showing the half-lives (in days) of key nuclear and mitochondrial proteins in neurons and myotubes.

(G) Model showing the TOM and SAM complexes in the OMM, and the MICOS complex in the IMM near the cristae junction. Tom40, Sam50, and Mic60 are in the core of the complexes, with Sam50 and Mic60 interacting with each other.

(H) Graph shows %old protein for day 0–8 for Tom40, Tom70, and Tom22 in myotubes.

(I) Graph shows %old protein for day 0–8 for Sam50, Mic60, Mic19, DnaJC11, Mic27, and Mic13 in myotubes.

For all graphs, the average whole-cell proteome is the dashed black line and the shaded gray area within dotted lines is the SD for the fraction. Error bars indicate SD. Data are an n = 3. *p < 0.05, **p < 0.001, ***p < 0.0001.

31 days, and the average whole-cell fraction has 25% old protein at day 8, with an SD spread of ~15%, with a class of mitochondrial proteins lie above this spread (Figures 2E and 2F). Remarkably, 40% of neuronal and myotube mitochondrial proteins detected in our study fall into the category of mitoLLPs. These mitoLLPs while longer lived than the average proteome, still turn over faster than nuclear LLPs that seem to be extremely stable. Moreover, the whole-cell and short-lived proteins (SLPs) in the neurons and myotubes have similar half-lives, suggesting that the primary difference between the two cell types is due to LLPs. Since we use human neurons and mouse myotubes, some of the slower turnover in neurons could be due to

Please cite this article in press as: Krishna et al., Identification of long-lived proteins in the mitochondria reveals increased stability of the electron transport chain, Developmental Cell (2021), https://doi.org/10.1016/j.devcel.2021.10.008

species-specific differences. However, comparison of our dataset with a previous study in cultured mouse neurons (Mathieson et al., 2018) demonstrates good correlation of half-lives for whole-cell (r = 0.65) and ETC proteins (r = 0.71), suggesting that our dataset is indeed comparable to mouse neurons.

To determine if mitoLLPs, similar to nuclear LLPs, can be part of large protein complexes, we looked at the translocase of the outer membrane (TOM), sorting and assembly machinery (SAM), and mitochondrial contact site and cristae-organizing system (MICOS) complexes, which are required for protein import, insertion, and cristae formation, respectively (Figure 2G). Due to better coverage of OMM proteins in myotubes compared with neurons, we used those datasets. We find that Tom40, a beta-barrel protein forming the central scaffold of the TOM complex, is longer lived ($T_{1/2}$: 7.4 days) compared with peripheral subunits Tom70 and Tom22 ($T_{1/2}$: 3.5 days) (Figure 2H). Similarly, Sam50 and Mic60, which are found in the central core of the SAM and MICOS complexes, respectively, are longer lived ($T_{1/2} \sim 8$ days) compared with the peripheral DnaJC11 and Mic13 ($T_{1/2} \sim 4$ days) (Figure 2I). Thus, similar to the NPC, these critical mitochondrial complexes also show heterogeneity in the turnover rate of their components with cores that are relatively stable (Figure S2I) (Toyama et al., 2013). We also find that the mito-ribosomal complex contains LLPs, with the 28S and 39S subunits clustering around a half-life of 6 days (Figure S2I). Interestingly, we find that ETC complexes CI and CIV show heterogeneous turnover with multiple LLPs and SLPs (Figures S2J, S2L, and S2N). In contrast, CIII and CV contain only LLPs, suggesting homogeneous turnover of the entire complex (Figures S2K, S2M, and S2N). Importantly, we see the same trend in neurons (Figure S2O), with a strong correlation between the half-lives of neuronal versus myotube ETC proteins (Figure S2P). Our data show that neuronal and myotube mitochondria exhibit higher longevity compared with other organelles and contain many LLPs that can be part of protein complexes. While some complexes have heterogeneous turnover that would require unique mechanisms to turn over the peripheral SLPs, others turn over homogeneously as a single unit.

Mitochondrial LLPs are core components of ETC complexes

Since the ETC contains multiple LLPs, we wanted to perform a detailed proteomic study of the respiratory chain that exists as ICs and higher-order SCs (Gu et al., 2016; Letts et al., 2016). While there is some previous evidence that SCs can increase the stability of the CI (Letts and Sazanov, 2017), the actual turnover rate of the ETC proteins in SCs has never been studied. Since our SILAC of mitochondrial fractions contained data from both ICs and SCs together, we used a blue-native page to isolate and identify SCs (Jha et al., 2016). Given the technical challenges in scaling up neuronal cultures for SC studies, we used myotubes for all further experiments. Consistent with previous studies, we observe a cluster of 4–5 bands at 1,000 kDa of higher-order SCs with varying stoichiometries of CI, CIII, and CIV (SCI,III_n,IV_n), along with individual CI, intermediate supercomplex ($SCIII_2,IV$), dimers of CIII and CIV ($CIII_2$ and CIV_2), and individual CIV and CII (Figure 3A, left gel, MYO) (Jha et al., 2016). We also confirmed the identity of these bands with an anti-oxphos cocktail, as well as CI, CIII, and CIV antibodies (Figure 3A, right blots). Interestingly, while dividing myoblasts also contain SCs, myotubes show an enrichment of both ICs and SCs (Figure 3A, DIV versus MYO). Differentiating myoblasts are known to undergo mitophagy and mitochondrial remodeling to increase oxphos (Sin et al., 2016), and this SC enrichment in myotubes could be another adaptation to increase mitochondrial respiration. This idea is supported by recent studies that show an increase in SCs during adipocyte differentiation and with exercise in skeletal muscles in human adults (Greggio et al., 2017; Hofmann et al., 2012).

To measure turnover, we ran the SILAC samples on blue-native gels, followed by mass spectrometry on higher-order SCs (SCI,III,IV), intermediate SC (SCIII,IV), dimers (III_2 and IV_2), individual CI and CII pooled (CI and II) and individual CIV (CIV). We confirmed their identity by quantifying protein abundance in each complex in the samples using normalized spectral abundance factor (NSAF) (Figure 3B) and determined their half-lives (Table S2). To effectively visualize the turnover rate, we color-coded the crystal structures of the complexes based on their half-lives ranging from 2 to 8 days (red to blue). We observed that subunits in the peripheral and membrane arms of the individual CI turnover at distinct rates, with the former turning over in a heterogeneous albeit rapid fashion with half-lives at ~3.7 days, while the latter turns over slower and homogenously with half-lives clustering around 6 days (Figures 3C and 3D). CI has 4 functional modules: N (NADH dehydrogenase), Q (electron transfer), Pp, and Pd (proton pumping) (Wirth et al., 2016). Our data show that the Pp and Pd modules in the membrane arm are long lived, with the Pd module half-lives clustering very tightly at 6 days (Figure 3E). Interestingly, the only protein in the membrane arm that shows rapid turnover is NDUFA11 (Figure 3C, back). It is worth noting that NDUFA11 interacts with CIII within the SCs, therefore it is conceivable that its rapid turnover could play a role in regulating this interaction and consequently the assembly/disassembly of SCs (Letts and Sazanov, 2017). CIII, which exists as a dimer ($CIII_2$) shows homogeneously blue subunits with core proteins MT-CYB1 and CYC1 being particularly long lived and UQCRC11 being the only short-lived red subunit (Figures 3F and 3H). Interestingly, CIV shows heterogeneous turnover with some SLPs (NDUFA4 and COX6B1) but also many LLPs such as COX6A1, MT-CO2, and COX7C (Figures 3G and 3H). Our data demonstrate that the ICs in myotubes have many LLPs and show unique turnover patterns—while CI has a stable core membrane arm and a short-lived peripheral arm, CIII is homogeneously long lived, and CIV shows generally heterogeneous turnover.

Differential stability of mitochondrial LLPs in ETC supercomplexes

We next generated half-lives and visualized higher-order and intermediate SC turnover by color coding the structure of the porcine respirasome (SCI,III_2,IV) since the mouse or human respirasome is unavailable (Figures 4A and S3F). We find that similar to the ICs, the peripheral arm of CI in the respirasome SC shows heterogeneous and fast turnover (Figure 4A). The membrane arm of CI, as well as $CIII_2$ and CIV, which are all membrane embedded, exhibit slower turnover (Figures 4A and S3A–S3D). Similar to the individual CI, NDUFA11 is the only membrane arm subunit that shows fast turnover (Figures

Please cite this article in press as: Krishna et al., Identification of long-lived proteins in the mitochondria reveals increased stability of the electron transport chain, Developmental Cell (2021), https://doi.org/10.1016/j.devcel.2021.10.008

CellPress

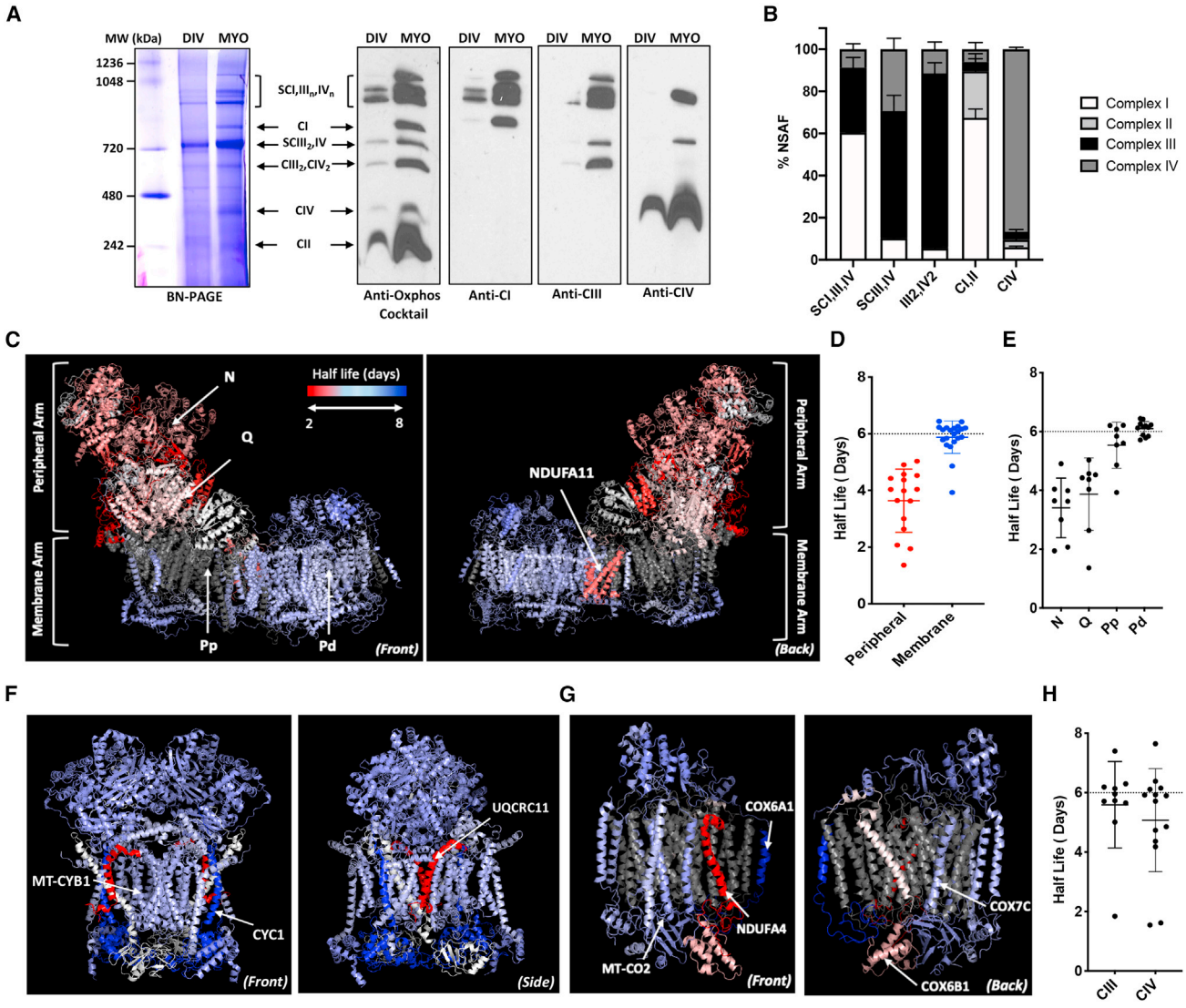

Figure 3. Mitochondrial LLPs are core components of the ETC complexes

(A) ETC complexes and supercomplexes in dividing myoblasts (DIV) versus myotubes (MYO). BN-PAGE gel (left) and western blots (right) with Anti-Oxphos cocktail, CI, CIII, and CIV antibodies show the bands corresponding to higher-order SCs (SCI,III$_n$,IV$_n$), individual CI (CI), intermediate SC (SCIII$_2$,IV), dimers of CIII and CIV (CIII$_2$, CIV$_2$), individual CIV (CIV), and individual CII (CII).

(B) Graph shows %NSAF abundance values of individual ETC complexes in the five gel band samples (SCI,III,IV), (SCIII,IV), (III$_2$,IV)$_2$, (CI,II), and (CIV).

(C) Turnover of CI subunits in the individual complex. Images show CI structure color-coded with protein half-lives from the front (left image) and back (right image). The peripheral and membrane arm, the N, Q, Pp, Pd modules, and subunit NDUFA11 are indicated.

(D) Dot plot shows the half-lives of the individual protein subunits in the peripheral and membrane arms of CI, respectively.

(E) Dot plot shows half-lives of individual protein subunits in the N, Q, Pp, and Pd modules of CI.

(F) Turnover of CIII$_2$ subunits in the individual dimeric complex. Images show CIII$_2$ structure color-coded with protein half-lives from the front (left image) and side (right image). Subunits MT-CYB1, CYC1, and UQCRC11 are indicated.

(G) Turnover of CIV subunits in the individual complex. Images show CIV structure color-coded with protein half-lives from the front (left image) and back (right image). Subunits MT-CO2, COX6A1, NDUFA4, COX7C, and COX6B1 are indicated.

(H) Dot plot shows half-lives of the individual subunits of CIII and CIV.

Scale of half-lives for all images is 2–8-days color-coded from dark red to white to dark blue. Proteins with no coverage are colored gray. For all graphs, a dotted line is drawn at the half-life of 6 days. Error bars indicate SD. Data are an n = 3.

S3A and S3B). NDUFA11 is shown to interact with UQCRB, UQCRQ, and UQCRH from CIII$_2$ (Gu et al., 2016; Letts et al., 2016), all of which are all long-lived stable proteins (Figure S3E, middle image). Indeed, many other proteins forming interactions between the different complexes within the respirasome are long lived and form stable contacts sites (Figure S3E, left, right image). In particular, COX7C, one of the most stable proteins in CIV, binds three LLPs in CI - MTND5, NDUFB9, and NDUFB7, suggesting a stable contact site for CI and CIV (Figure 5A).

Please cite this article in press as: Krishna et al., Identification of long-lived proteins in the mitochondria reveals increased stability of the electron transport chain, Developmental Cell (2021), https://doi.org/10.1016/j.devcel.2021.10.008

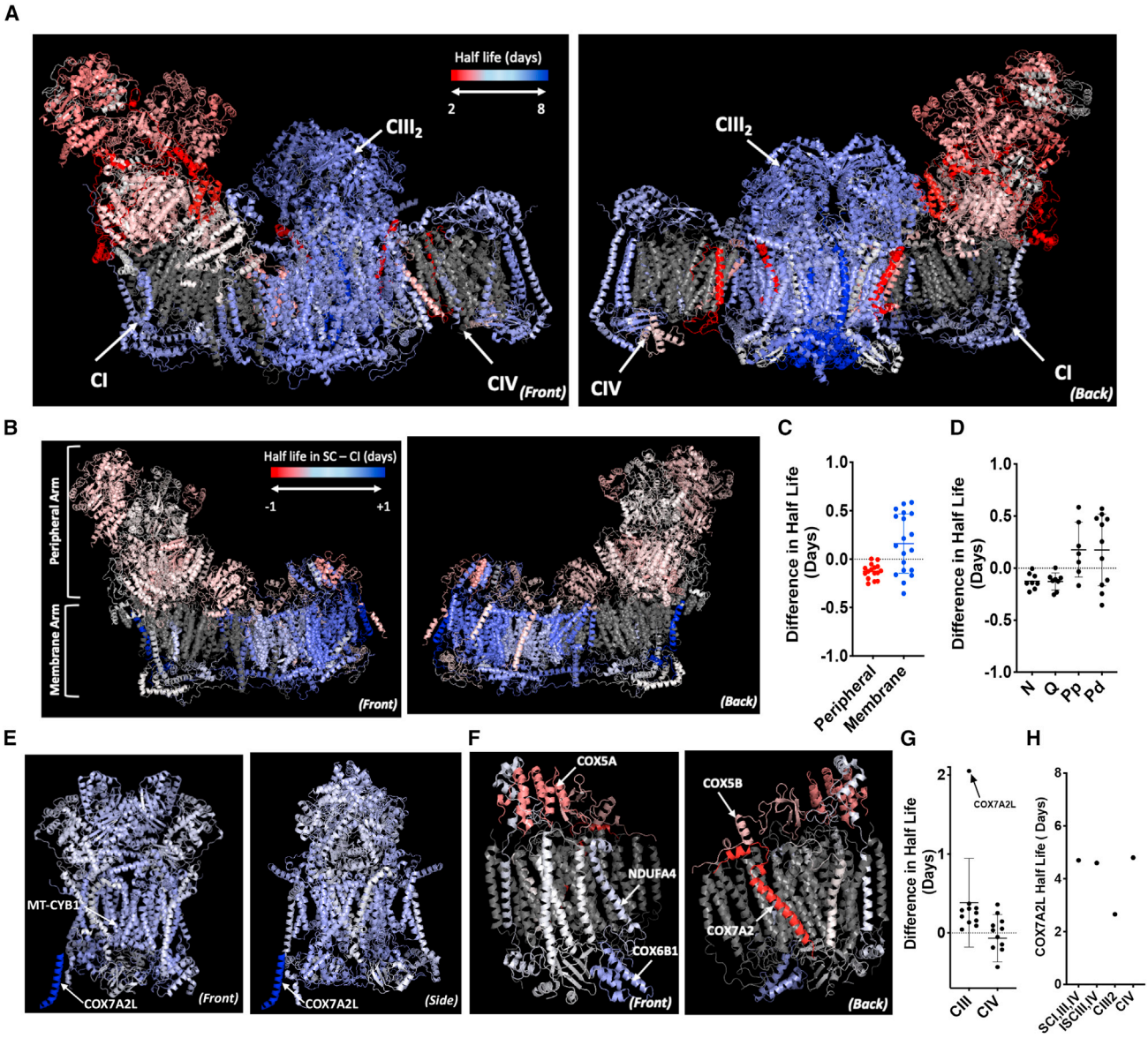

Figure 4. Differential stability of mitochondrial LLPs in ETC supercomplexes

(A) Turnover of subunits in the respirasome SC. Images show the porcine respirasome structure with protein half-lives color-coded in the range of 2–8 days from dark red to white to dark blue from the front (left image) and back (right image). CI, $CIII_2$, and CIV are indicated.

(B) Differential turnover between SCs and individual CI. Images show CI structure color-coded using a half-life subtraction of SC-CI. The peripheral and membrane arms are indicated.

(C) Dot plot shows the difference in half-lives of the individual protein subunits in the peripheral and membrane arms between SC-CI.

(D) Dot plot shows difference in half-lives of the individual protein subunits in the N, Q, Pp, and Pd modules between SC and CI.

(E) Differential turnover between SCs and $CIII_2$. Images show $CIII_2$ structure color-coded using a half-life subtraction of SC-$CIII_2$. COX7A2L is not present in the PDB structure and is added manually at the side of $CIII_2$. MT-CYB1 and COX7A2L are indicated.

(F) Differential turnover between SCs and CIV. Images show CIV structure color-coded using a half-life subtraction of SC-CIV. Subunits COX5A, NDUFA4, COX6B1, COX5B, and COX7A2 are indicated.

(G) Dot plot shows the difference in half-lives of the protein subunits in the $CIII_2$ and CIV between SC-$CIII_2$ and SC-CIV, respectively. COX7A2L is indicated on the graph.

(H) Half-life of COX7A2L in supercomplexes (SCI,III,IV), intermediate supercomplex (ISCIII,IV), $CIII_2$, and CIV.

Scale for differential turnover structures is −1 to +1 days from dark red to white to dark blue representing faster turnover in SCs to slower turnover in SCs. Proteins with no coverage are colored gray. For all graphs, a dotted line is drawn at the half-life difference of 0 days. Error bars indicate SD. Data are an n = 3.

Please cite this article in press as: Krishna et al., Identification of long-lived proteins in the mitochondria reveals increased stability of the electron transport chain, Developmental Cell (2021), https://doi.org/10.1016/j.devcel.2021.10.008

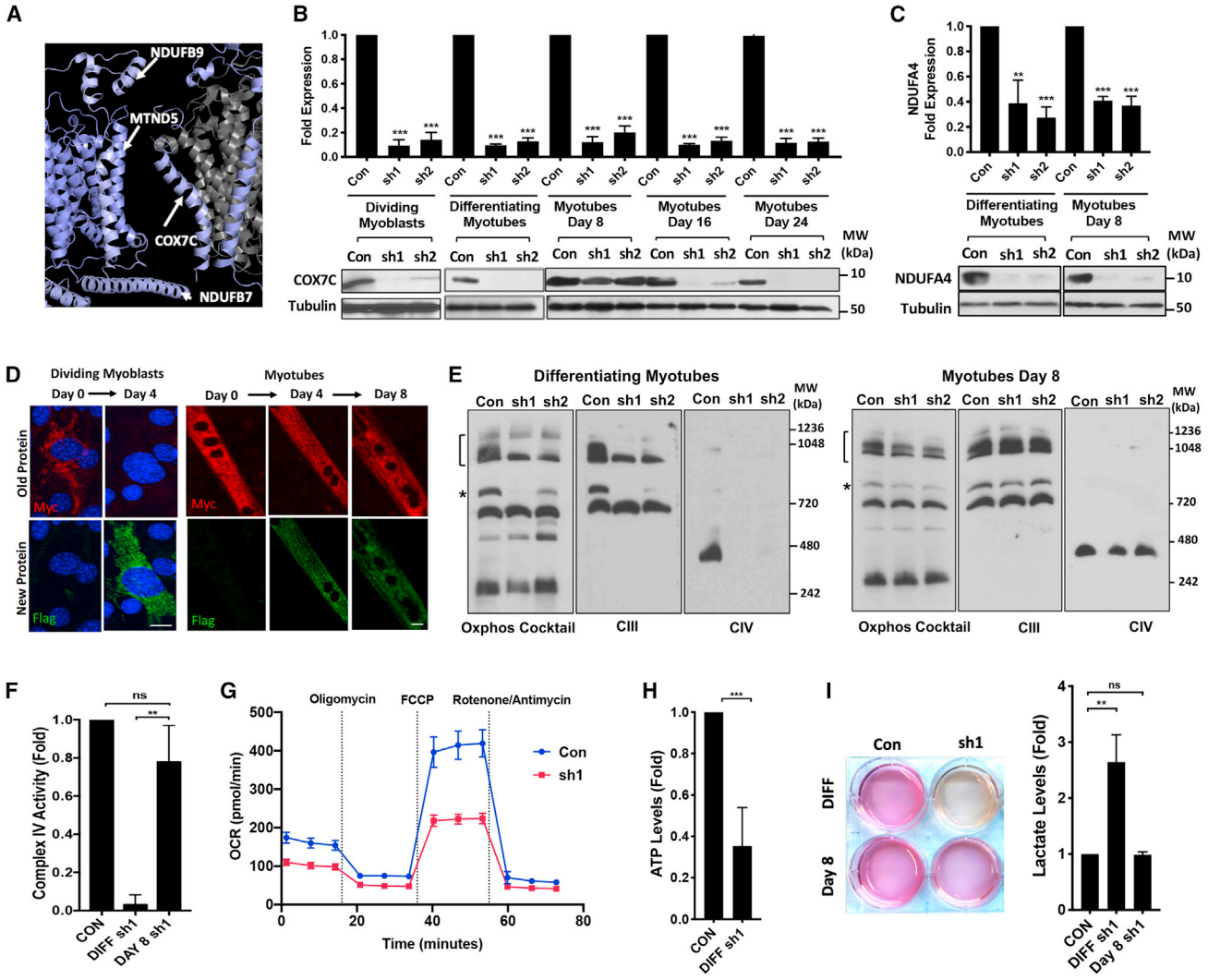

Figure 5. Longevity of COX7C protects myotubes from loss-of-function defects in complex IV and supercomplex assembly

(A) LLP COX7C from CIV forms a stable contact site with CI by interacting with long-lived subunits NDUFB9, MTND5, and NDUFB7 in the respirasome SC. Image shows subunits in the contact site with half-lives color-coded from 2–8 days from dark red to white to dark blue. Proteins with no coverage are colored gray.

(B) COX7C mRNA levels (qPCR, top panel) and protein levels (western blot, bottom panels) with control and COX7C-hairpins (sh1,sh2) in dividing myoblasts, differentiating myotubes, fully differentiated myotubes at day 8, 16, and 24.

(C) NDUFA4 mRNA levels (top panel) and protein levels (bottom panel) with control and NDUFA4-hairpins (sh1,sh2) in differentiating myotubes and fully differentiated myotubes at day 8. Western blots show tubulin as loading control.

(D) COX7C turnover as measured by RITE. Images show Myc tag (old protein, top panel) and FLAG tag (new protein, bottom panel) at day 0 and 4 in dividing myoblasts (left) and day 0, 4, and 8 in myotubes (right).

(E) ETC SC and IC levels in control and COX7C hairpins. Western blots show levels of all the complexes (oxphos cocktail), CIII and CIV containing complexes in differentiating myotubes (left blots), and day 8 myotubes (right blots). Bracket indicates higher-order SCs, and asterisk indicates the intermediate SC.

(F) CIV activity in control and sh1-mediated COX7C knockdown in differentiating myotubes or day 8 myotubes.

(G) Oxygen consumption rates (OCRs) in pmol/min over a seahorse assay of 80 min and in control and sh1-COX7C knockdowns in differentiating myotubes. Injection timings of oligomycin, FCCP, and rotenone/antimycin are indicated with dotted lines.

(H) ATP levels in control and sh1-COX7C knockdowns in differentiating myotubes.

(I) Left, image of cell culture media in a 6-well plate, and right, graph of fold change in lactate levels in control and sh1-COX7C knockdowns in differentiating myotubes or day 8 myotubes.

For all graphs, error bars represent SD from an n = 3. **p < 0.01, ***p < 0.001. Scale bars, 10 μm. Western blot markers are indicated.

To compare the turnover of SCs versus ICs, we subtracted the half-lives of proteins in the SCs from their respective half-lives in the ICs and then color-coded them on the scale of −1 to +1 days (red to blue). Remarkably, we find that while turnover in the peripheral arm of CI is relatively similar between the SCs and ICs, the majority of the membrane arm of CI exhibits more longevity in the SCs (Figure 4B). Indeed, most subunits in the membrane arm (consisting of Pp and Pd modules) show a 0.5 days or 12 h delay in turnover (Figures 4C and 4D). Interestingly, only the LLPs in CI display this increased stability, while the

Please cite this article in press as: Krishna et al., Identification of long-lived proteins in the mitochondria reveals increased stability of the electron transport chain, Developmental Cell (2021), https://doi.org/10.1016/j.devcel.2021.10.008

shorter-lived proteins do not. Similarly, we find that $CIII_2$ is also more stable in SCs as well as in the intermediate SC, with many subunits exhibiting the 0.5 days delay (Figures 4E, 4G, and S4A). This is the first direct evidence based on protein turnover data establishing that CI and $CIII_2$ are more stable in SCs. Moreover, we find that the subunit COX7A2L is more stable in the SCs by 2 days, the largest difference observed for any ETC subunit (Figures 4E and 4G). Interestingly, COX7A2L has been reported to bind to $CIII_2$ to promote the assembly of intermediate $SCIII_2$,IV and the respirasome SCI,III_2,IV, and its loss-of-function leads to reduced SC formation (Cogliati et al., 2016; Lobo-Jarne et al., 2018). We see that COX7A2L has a half-life of 2.5 days in $CIII_2$, which increases to 4.8 days in SCI,III,IV, ISCIII,IV, and CIV (Figure 4H). This increased stability could be due to its structural location as it binds directly with $CIII_2$ to facilitates its interaction with CIV and CI, making it peripheral in $CIII_2$ but buried deep inside the SCs and less accessible for degradation. Unlike CI and $CIII_2$, CIV shows a different stability pattern in the SCs versus IC. We find that SLPs such as COX6B1 and NDUFA4 are more stable in the SCs, while LLPs like COX5A and COX5B are more stable in the IC (Figures 4F and 4G). We also find that CIV subunits are more stable in the SCs compared with the intermediate SC, while the CIV_2 is more stable than monomeric CIV (Figures S4B–S4E). These results show that LLPs are core components of SCs, also forming stable contact sites between the different complexes that could be essential for maintaining its quaternary structure. Our study also shows that ETC proteins exhibit differential stability in SCs versus ICs, particularly CI and $CIII_2$, where the LLPs show increased longevity in the SCs.

Longevity of COX7C protects myotubes from loss-of-function defects in complex IV and supercomplex assembly

Since LLPs are core components of protein complexes, we hypothesize that under conditions that lead to a decline in their transcription, they could function as a scaffold for the structural and functional integrity of the complex. We decided to uncouple protein levels and function of a mitoLLP in the ETC from its transcription by depleting its mRNA. We picked COX7C as it is one of the longest-lived proteins in CIV (Figure 3G, $T_{1/2}$: 6 days) and also forms critical interactions with three LLPs from CI in the respirasome, suggesting that this is one of the most stable contact points within the SC (Figure 5A). Also, the function of COX7C is currently unknown, and it has been reported to undergo an age-dependent decline in transcription in human skeletal muscles (Su et al., 2015).

To deplete COX7C, we used miRE-inducible knockdowns in three cell systems—dividing myoblasts, differentiating myotubes, and fully differentiated myotubes (knockdowns were induced post-differentiation for 8, 16, and 24 days) and determined COX7C mRNA and protein levels. Dividing and differentiating cells show a dramatic reduction in COX7C mRNA as well as protein levels (Figure 5B). Interestingly, while myotubes at day 8 clearly show a reduction of COX7C at the transcript level, they show minimal change in the protein level (Figure 5B). Importantly, by day 16, we start seeing a reduction of COX7C protein, with complete depletion by day 24, to the same extent as seen with differentiating myotubes (Figure 5B). To validate that this effect was indeed due to the long-lived nature of the protein and not due to any defects in COX7C degradation or the RNAi machinery, we knocked down another LLP as well as an SLP from CIV. Similar to COX7C, COX5A knockdowns ($T_{1/2}$:6 days) show a clear reduction of mRNA and protein levels in differentiating myotubes, and knockdowns in day 8 myotubes show a reduction of mRNA levels while having minimal effect on the protein levels (Figure S5A). Importantly, knockdowns of short-lived CIV protein NDUFA4 ($T_{1/2}$:1.8 days) show a clear reduction of RNA as well as protein levels in both differentiating and day 8 myotubes (Figure 5C). These data demonstrate that COX7C and COX5A are indeed long lived in post-mitotic myotubes. To further validate COX7C's longevity, we imaged old COX7C protein in the cell using RITE. We find that in dividing myoblasts by day 4 old COX7C protein (Myc) is down to less than 20%, and mostly new protein is present (FLAG) (Figures 5D, S5B, and S5C), indicating a short half-life. However, in myotubes, there is a persistence of old protein at day 4 and even day 8 (55% and 40%, respectively) despite production of new protein (Figures 5D, S5B, and S5C), validating that COX7C has a longer half-life in myotubes.

We next examined the function of COX7C, and the role of its longevity in maintaining that function in myotubes. Intriguingly, we find that COX7C knockdowns in differentiating myotubes show a substantial depletion of CIV, intermediate as well as higher-order SC levels (Figures 5E and S5D). This indicates that COX7C might be involved in the assembly or stability of CIV, which subsequently leads to loss of SCs as well. We also find a dramatic reduction in CIV enzymatic activity, oxygen consumption, and ATP levels with the knockdowns in differentiating myotubes (Figures 5F–5H). Additionally, we also noted that the color of the culture media changed from pink to yellow with the knockdowns due to increased lactate production (Figure 5I) and extracellular acidification rate (Figure S5H). This indicates that COX7C-depleted cells shunt to glycolysis because of impaired ETC function. Importantly, these cells also show a reduction in myotube thickness (Figures S5I and S5J) indicating that COX7C-dependent respiration is critical for myotube health. Interestingly, knockdowns in day 8 myotubes do not show any reduction in CIV or SC levels (Figures 5E and S5E). Also, the day-8 knockdown has the same the CIV enzymatic activity as control cells (Figure 5F), and the culture media stays pink, with lactate levels similar to control cells (Figure 5I). Thus, despite depletion of COX7C transcripts, the longevity of this protein is able to protect myotubes from its loss-of-function defects in CIV/SC assembly, thereby maintaining CIV activity and ETC function. Indeed, only at day 16 and 24 when the levels of the protein start to get depleted do we see a reduction in the levels of CIV and SCs (Figures S5F and S5G). Therefore, we have demonstrated a critical role for COX7C in CIV and SC assembly and have established that its longevity can maintain ETC integrity despite a decline in its mRNA. Given that the majority of the ETC is long lived and is known to undergo age-dependent transcriptional decline in post-mitotic cells (Su et al., 2015), our study provides an exciting link between mitoLLPs in protein complexes and aging.

DISCUSSION

A critical finding of our study is that LLPs show differential stability in SCs. Previous studies have shown that mutations in

Please cite this article in press as: Krishna et al., Identification of long-lived proteins in the mitochondria reveals increased stability of the electron transport chain, Developmental Cell (2021), https://doi.org/10.1016/j.devcel.2021.10.008

CIII and CIV can affect CI activity, suggesting that SCs can increase CI stability (Acín-Pérez et al., 2004; Diaz et al., 2006). However, we provide the first half-life measurements that demonstrate increased stability of CI as well as $CIII_2$ in the SCs. These data establish a clear function of respiratory SCs in myotubes. Although it is only an increase of 0.5 days, given that the ETC functions in the scale of milliseconds (electron transfer takes 5–20 ms), a 12-h difference could easily lead to increased respiratory output. While SCs do not affect the actual rate of electron transfer between the complexes (Fedor and Hirst, 2018), their increased stability could cause electron transfer to occur for longer. Interestingly, only the LLPs of CI and $CIII_2$ show this increased stability, lending further support to our hypothesis that LLPs are critical for protein complex stability and function. Also, in CIV the shorter-lived subunits are more stable in the SCs, and vice versa, suggesting that there could be specialized functions of these proteins in the SCs and ICs, respectively.

We also provide the first observation of age mosaicism in mitochondria, similar to what we have previously observed with NPCs (Toyama et al., 2019), primary cilia, and pancreatic beta cells (Arrojo et al., 2019). This raises a key question: do the distinct mitochondrial populations have differences in structure, composition, and function? Interestingly, mitochondria in the same cell can exhibit extensive heterogeneity in membrane potential, respiratory capacity, and ROS production (Kuznetsov and Margreiter, 2009). Indeed, perinuclear clustering of aged mitochondria has been observed in stem cells before cell division (Katajisto et al., 2015). Moreover, perinuclear mitochondria in cardiomyocytes can drive ATP synthesis for nuclear import (Dzeja et al., 2002). It is conceivable that the clusters of old mitochondria we observe in neurons could have specialized functions, particularly for the axonal mitochondria at synapses. While we observed that axonal mitochondria tend to be older *in vivo*, we did not observe a consistent similar polarization in the cultured neurons, most likely because they require further maturation or glial cell co-culture to establish this polarity. Our MIMS-EM data also show that neurons have older mitochondria than muscle fibers, which could be because muscle fibers have quiescent satellite cells that when activated during injury and development can divide and fuse into the fiber (Yin et al., 2013). Since quiescent myoblasts *in vitro* display faster turnover of most nuclear LLPs (Toyama et al., 2019), the satellite cells *in vivo* could have newer mitochondria that undergo fusion/fission cycles with the muscle mitochondria to reduce the $^{15}N/^{14}N$.

An important finding from our study is the distinction between nuclear and mitoLLPs, as the former turnover extremely slowly with half-lives of a month, while the latter turn over in a week. This is corroborated *in vivo* where nuclear proteins persist for a year, and mitochondrial proteins can persist for a month (Fornasiero et al., 2018; Karunadharma et al., 2015; Toyama et al., 2013). Our half-lives are in contrast with the *in vivo* studies because while our cells are post-mitotic, they are not fully mature neurons or muscle fibers and can only be cultured for a few weeks. Indeed, a previous study that compared *in vivo* and *in vitro* data showed that half-lives are lower in the latter (Fornasiero et al., 2018). While the half-lives generated in our system may be scaled down, the relative turnover among LLPs is similar. Indeed, an *in vivo* study categorized proteins that are above 98th percentile in terms of stability as "exceptional LLPs" (histones and nups), whereas the 95–98th percentile were "normal LLPs" (containing signaling, SNARE and mitochondrial proteins) (Fornasiero et al., 2018). We also find a strong correlation in the half-lives of ETC proteins between our *in vitro* and this *in vivo* dataset of brain and heart tissues ($r = 0.75$, $p < 0.001$) (Fornasiero et al., 2018). We speculate that some of the differences in the data could be due to the cell systems used or by the use of tissue homogenates in previous studies instead of separating the mitochondrial fraction and ETC complexes. Since proteins show differential stability in SCs, it is indeed critical to separate the complexes for ETC turnover studies.

A key finding of our study is that 40% of mitochondrial proteins are LLPs. This suggests that mitochondria have evolved to be longer lived than the cellular proteome, an adaptation that has vital implications for the role of LLPs. While previous work has described a link between nuclear LLPs and their role in aging (D'Angelo et al., 2009), an open question is that why would a cell have mitoLLPs, given that their longevity makes them more susceptible to oxidative damage from the ETC? Our COX7C data suggests that mitoLLPs are insulated against changes in their gene expression as the complexes will still contain the old protein and therefore function effectively. Thus, we speculate that a critical role for LLPs could be maintaining protein complex function in conditions of cellular stress where global transcription/translation is diminished. Indeed, transient stressors such as heat shock and starvation can lead to a decline in transcriptional and translational rates (Mahat et al., 2016; Pain, 1994). More importantly, during aging, there is a global decline in gene expression, particularly of mitochondrial and ETC proteins (Su et al., 2015). It is conceivable that during these conditions the peripheral SLPs in a complex would fall off, but the core LLPs would be present and could maintain a functional subcomplex to slow down cellular deterioration. Moreover, such heterogeneity in the complex could also function to modulate the activity of protein complexes for adapting to different conditions without having to dismantle the long-lived scaffold.

Limitations of the study

While we identify mitoLLPs *in vitro*, a limitation is that the study lacks correlative proteomics data *in vivo*. Also, it is unclear if longevity of LLPs compared with SLPs can protect mitochondrial function during specific cellular stress conditions and aging. Some of these questions could not be addressed due to technical and experimental delays caused by the COVID-19 pandemic.

STAR★METHODS

Detailed methods are provided in the online version of this paper and include the following:

- KEY RESOURCES TABLE
- RESOURCE AVAILABILITY
  - Lead contact
  - Materials availability
  - Data and code availability

- EXPERIMENTAL MODEL AND SUBJECT DETAILS
  - Mouse
  - Cell Culture
- METHOD DETAILS
  - Stable isotope metabolic labelling of mammals (SILAM)
  - Sample processing for Scanning Electron Microscopy imaging
  - Multi-isotope mass spectroscopy and scanning electron microscopy
  - Stable isotope labeling by amino acids in cell culture (SILAC)
  - Fractionation and LC/MS Analysis
  - BN-PAGE and western blots
  - Gel Band Extraction and LC/MS Analysis
  - shRNA construction, lentiviral generation and knockdowns
  - qPCR
  - Western Blotting
  - RITE plasmid generation, tag switching and immunofluorescence
  - Mitochondrial functional assays
- QUANTIFICATION AND STATISTICAL ANALYSIS
  - MIMS image analysis, alignment and quantification
  - Mass spectrometry data analysis and peptide filtration
  - Half-life calculation
  - NSAF analysis
  - Half-life visualization of crystal structures
  - RITE & Myotube Image Analysis
  - Statistical methods and representative figures

SUPPLEMENTAL INFORMATION

Supplemental information can be found online at https://doi.org/10.1016/j.devcel.2021.10.008.

ACKNOWLEDGMENTS

This work is supported by NIH Transformative Research Award grant R01 NS096786, Keck Foundation, NOMIS Foundation, NGS Core Facility, Razavi Newman Integrative Genomics, Bioinformatics Core Facility of the Salk Institute (NIH-NCI CCSG: P30 014195), Compton Foundation, Helmsley Charitable Trust, Flow Cytometry Core Facility of the Salk Institute (NIH-NCI CCSG: P30 014195), Mass Spectrometry Core of the Salk Institute (NIH-NCI CCSG: P30 014195), Helmsley Center for Genomic Medicine and Salk Women and Science. This work is also supported by NIH R24GM137200 and U24NS120055 and NSF - NSF2014862-UTA20-000890. The authors thank J. Moresco, J. Diedrich, and A. Pinto for technical support with Mass Spectometry (Salk Institute), J. Letts (University of California, Davis), and D. Butler (Salk Institute) for codes for Pymol half-life structures, S. Schafer and F. Gage (Salk Institute) for hES cells and G. Shadel and members of the Shadel Lab (Salk Institute) for help with mitochondrial assays. Graphical abstract created with Biorender.com.

AUTHOR CONTRIBUTIONS

S.K. and M.H. designed the study and wrote the paper. S.K. performed the experiments and analyzed the data. R.A.D., M.E., and M.H. designed the SILAM and MIMS-EM study. R.A.D. performed the SILAM and MIMS-EM study. R.A.D. and R.R. contributed assistance in MIMS data analysis. R.R. created the MesoFusion plugin. J.S.C. assisted in neuronal SILAC experiments and data analysis and generated the models for half-life calculations. J.S.C., R.A.D., R.R., and M.E. assisted in writing the paper.

DECLARATION OF INTERESTS

The authors declare no competing interests.

Received: September 28, 2020
Revised: July 28, 2021
Accepted: October 8, 2021
Published: October 28, 2021

REFERENCES

Acín-Pérez, R., Bayona-Bafaluy, M.P., Fernández-Silva, P., Moreno-Loshuertos, R., Pérez-Martos, A., Bruno, C., Moraes, C.T., and Enríquez, J.A. (2004). Respiratory complex III is required to maintain complex I in mammalian mitochondria. Mol. Cell *13*, 805–815.

Adams, S.R., Mackey, M.R., Ramachandra, R., Palida Lemieux, S.F., Steinbach, P., Bushong, E.A., Butko, M.T., Giepmans, B.N.G., Ellisman, M.H., and Tsien, R.Y. (2016). Multicolor electron microscopy for simultaneous visualization of multiple molecular species. Cell Chem. Biol. *23*, 1417–1427.

Arrojo, E.D.R., Lev-Ram, V., Tyagi, S., Ramachandra, R., Deerinck, T., Bushong, E., Phan, S., Orphan, V., Lechene, C., Ellisman, M.H., and Hetzer, M.W. (2019). Age mosaicism across multiple scales in adult tissues. Cell Metab. *30*, 343–351.e3.

Benninghoven, A., Rudenauer, F.G., and Werner, H.W. (1987). Secondary Ion Mass Spectrometry : Basic Concepts, Instrumental Aspects, Applications, and Trends (Wiley).

Bezawork-Geleta, A., Brodie, E.J., Dougan, D.A., and Truscott, K.N. (2015). LON is the master protease that protects against protein aggregation in human mitochondria through direct degradation of misfolded proteins. Sci. Rep. *5*, 17397.

Buchwalter, A., Schulte, R., Tsai, H., Capitanio, J., and Hetzer, M. (2019). Selective clearance of the inner nuclear membrane protein emerin by vesicular transport during ER stress. eLife *8*, e497–96.

Cheung, Y.T., Lau, W.K., Yu, M.S., Lai, C.S., Yeung, S.C., So, K.F., and Chang, R.C. (2009). Effects of all-trans-retinoic acid on human SH-SY5Y neuroblastoma as in vitro model in neurotoxicity research. Neurotoxicology *30*, 127–135.

Clayton, D.A., and Shadel, G.S. (2014). Isolation of mitochondria from cells and tissues. Cold Spring Harb. Protoc. *2014*, pdb.top074542.

Cogliati, S., Calvo, E., Loureiro, M., Guaras, A.M., Nieto-Arellano, R., Garcia-Poyatos, C., Ezkurdia, I., Mercader, N., Vázquez, J., and Enriquez, J.A. (2016). Mechanism of super-assembly of respiratory complexes III and IV. Nature *539*, 579–582.

D'Angelo, M.A., Raices, M., Panowski, S.H., and Hetzer, M.W. (2009). Age-dependent deterioration of nuclear pore complexes causes a loss of nuclear integrity in postmitotic cells. Cell *136*, 284–295.

David, D.C., Ollikainen, N., Trinidad, J.C., Cary, M.P., Burlingame, A.L., and Kenyon, C. (2010). Widespread protein aggregation as an inherent part of aging in C. elegans. PLoS Biol. *8*, e1000450.

Diaz, F., Fukui, H., Garcia, S., and Moraes, C.T. (2006). Cytochrome c oxidase is required for the assembly/stability of respiratory complex I in mouse fibroblasts. Mol. Cell. Biol. *26*, 4872–4881.

Dzeja, P.P., Bortolon, R., Perez-Terzic, C., Holmuhamedov, E.L., and Terzic, A. (2002). Energetic communication between mitochondria and nucleus directed by catalyzed phosphotransfer. Proc. Natl. Acad. Sci. USA *99*, 10156–10161.

Fedor, J.G., and Hirst, J. (2018). Mitochondrial supercomplexes do not enhance catalysis by quinone channeling. Cell Metab. *28*, 525–531.e4.

Fellmann, C., Hoffmann, T., Sridhar, V., Hopfgartner, B., Muhar, M., Roth, M., Lai, D.Y., Barbosa, I.A., Kwon, J.S., Guan, Y., et al. (2013). An optimized microRNA backbone for effective single-copy RNAi. Cell Rep. *5*, 1704–1713.

Fornasiero, E.F., Mandad, S., Wildhagen, H., Alevra, M., Rammner, B., Keihani, S., Opazo, F., Urban, I., Ischebeck, T., Sakib, M.S., et al. (2018). Precisely measured protein lifetimes in the mouse brain reveal differences across tissues and subcellular fractions. Nat. Commun. *9*, 4230.

Greggio, C., Jha, P., Kulkarni, S.S., Lagarrigue, S., Broskey, N.T., Boutant, M., Wang, X., Conde Alonso, S., Ofori, E., Auwerx, J., et al. (2017). Enhanced

respiratory chain supercomplex formation in response to exercise in human skeletal muscle. Cell Metab. *25*, 301–311.

Gu, J., Wu, M., Guo, R., Yan, K., Lei, J., Gao, N., and Yang, M. (2016). The architecture of the mammalian respirasome. Nature *537*, 639–643.

He, L., Diedrich, J., Chu, Y.Y., and Yates, J.R., 3rd. (2015). Extracting accurate precursor information for tandem mass spectra by RawConverter. Anal. Chem. *87*, 11361–11367.

Hipp, M.S., Kasturi, P., and Hartl, F.U. (2019). The proteostasis network and its decline in ageing. Nat. Rev. Mol. Cell Biol. *20*, 421–435.

Hofmann, A.D., Beyer, M., Krause-Buchholz, U., Wobus, M., Bornhäuser, M., and Rödel, G. (2012). OXPHOS supercomplexes as a hallmark of the mitochondrial phenotype of adipogenic differentiated human MSCs. PLoS One *7*, e35160.

Jha, P., Wang, X., and Auwerx, J. (2016). Analysis of mitochondrial respiratory chain supercomplexes using blue native polyacrylamide gel electrophoresis (BN-PAGE). Curr. Protoc. Mouse Biol. *6*, 1–14.

Karunadharma, P.P., Basisty, N., Chiao, Y.A., Dai, D.F., Drake, R., Levy, N., Koh, W.J., Emond, M.J., Kruse, S., Marcinek, D., et al. (2015). Respiratory chain protein turnover rates in mice are highly heterogeneous but strikingly conserved across tissues, ages, and treatments. FASEB J *29*, 3582–3592.

Katajisto, P., Döhla, J., Chaffer, C.L., Pentinmikko, N., Marjanovic, N., Iqbal, S., Zoncu, R., Chen, W., Weinberg, R.A., and Sabatini, D.M. (2015). Stem cells. Asymmetric apportioning of aged mitochondria between daughter cells is required for stemness. Science *348*, 340–343.

Keene, D.R. (2015). A review of color blindness for microscopists: guidelines and tools for accommodating and coping with color vision deficiency. Microsc. Microanal. *21*, 279–289.

Knott, S.R.V., Maceli, A., Erard, N., Chang, K., Marran, K., Zhou, X., Gordon, A., Demerdash, O.E., Wagenblast, E., Kim, S., et al. (2014). A computational algorithm to predict shRNA potency. Mol. Cell *56*, 796–807.

Kuznetsov, A.V., and Margreiter, R. (2009). Heterogeneity of mitochondria and mitochondrial function within cells as another level of mitochondrial complexity. Int. J. Mol. Sci. *10*, 1911–1929.

Letts, J.A., Fiedorczuk, K., and Sazanov, L.A. (2016). The architecture of respiratory supercomplexes. Nature *537*, 644–648.

Letts, J.A., and Sazanov, L.A. (2017). Clarifying the supercomplex: the higher-order organization of the mitochondrial electron transport chain. Nat. Struct. Mol. Biol. *24*, 800–808.

Lobo-Jarne, T., Nývltová, E., Pérez-Pérez, R., Timón-Gómez, A., Molinié, T., Choi, A., Mourier, A., Fontanesi, F., Ugalde, C., and Barrientos, A. (2018). Human COX7A2L regulates Complex III biogenesis and promotes supercomplex organization remodeling without affecting mitochondrial bioenergetics. Cell Rep. *25*, 1786–1799.e4.

López-Otín, C., Blasco, M.A., Partridge, L., Serrano, M., and Kroemer, G. (2013). The hallmarks of aging. Cell *153*, 1194–1217.

Mahat, D.B., Salamanca, H.H., Duarte, F.M., Danko, C.G., and Lis, J.T. (2016). Mammalian heat shock response and mechanisms underlying its genome-wide transcriptional regulation. Mol. Cell *62*, 63–78.

Mathieson, T., Franken, H., Kosinski, J., Kurzawa, N., Zinn, N., Sweetman, G., Poeckel, D., Ratnu, V.S., Schramm, M., Becher, I., et al. (2018). Systematic analysis of protein turnover in primary cells. Nat. Commun. *9*, 689.

Moehle, E.A., Shen, K., and Dillin, A. (2019). Mitochondrial proteostasis in the context of cellular and organismal health and aging. J. Biol. Chem. *294*, 5396–5407.

Pain, V.M. (1994). Translational control during amino acid starvation. Biochimie *76*, 718–728.

Palikaras, K., Lionaki, E., and Tavernarakis, N. (2018). Mechanisms of mitophagy in cellular homeostasis, physiology and pathology. Nat. Cell Biol. *20*, 1013–1022.

Park, S.K., Aslanian, A., McClatchy, D.B., Han, X., Shah, H., Singh, M., Rauniyar, N., Moresco, J.J., Pinto, A.F., Diedrich, J.K., et al. (2014). Census 2: isobaric labeling data analysis. Bioinformatics *30*, 2208–2209.

Peng, J., Elias, J.E., Thoreen, C.C., Licklider, L.J., and Gygi, S.P. (2003). Evaluation of multidimensional chromatography coupled with tandem mass spectrometry (LC/LC-MS/MS) for large-scale protein analysis: the yeast proteome. J. Proteome Res. *2*, 43–50.

Perez-Riverol, Y., Csordas, A., Bai, J., Bernal-Llinares, M., Hewapathirana, S., Kundu, D.J., Inuganti, A., Griss, J., Mayer, G., Eisenacher, M., et al. (2019). The PRIDE database and related tools and resources in 2019: improving support for quantification data. Nucleic Acids Res. *47*, D442–D450.

Picca, A., Guerra, F., Calvani, R., Coelho-Junior, H.J., Bossola, M., Landi, F., Bernabei, R., Bucci, C., and Marzetti, E. (2020). Generation and release of mitochondrial-derived vesicles in health, aging and disease. J. Clin. Med. *9*, 1440.

Price, J.C., Guan, S., Burlingame, A., Prusiner, S.B., and Ghaemmaghami, S. (2010). Analysis of proteome dynamics in the mouse brain. Proc. Natl. Acad. Sci. USA *107*, 14508–14513.

Savas, J.N., Toyama, B.H., Xu, T., Yates, J.R., 3rd, and Hetzer, M.W. (2012). Extremely long-lived nuclear pore proteins in the rat brain. Science *335*, 942.

Schafer, S.T., Paquola, A.C.M., Stern, S., Gosselin, D., Ku, M., Pena, M., Kuret, T.J.M., Liyanage, M., Mansour, A.A., Jaeger, B.N., et al. (2019). Pathological priming causes developmental gene network heterochronicity in autistic subject-derived neurons. Nat. Neurosci. *22*, 243–255.

Schneider, C.A., Rasband, W.S., and Eliceiri, K.W. (2012). NIH Image to ImageJ: 25 years of image analysis. Nat. Methods *9*, 671–675.

Shpilka, T., and Haynes, C.M. (2018). The mitochondrial UPR: mechanisms, physiological functions and implications in ageing. Nat. Rev. Mol. Cell Biol. *19*, 109–120.

Sin, J., Andres, A.M., Taylor, D.J., Weston, T., Hiraumi, Y., Stotland, A., Kim, B.J., Huang, C., Doran, K.S., and Gottlieb, R.A. (2016). Mitophagy is required for mitochondrial biogenesis and myogenic differentiation of C2C12 myoblasts. Autophagy *12*, 369–380.

Song, J., Herrmann, J.M., and Becker, T. (2021). Quality control of the mitochondrial proteome. Nat. Rev. Mol. Cell Biol. *22*, 54–70.

Sorzano, C.O., Thévenaz, P., and Unser, M. (2005). Elastic registration of biological images using vector-spline regularization. IEEE Trans. Biomed. Eng. *52*, 652–663.

Sosinsky, G.E., Deerinck, T.J., Greco, R., Buitenhuys, C.H., Bartol, T.M., and Ellisman, M.H. (2005). Development of a model for microphysiological simulations: small nodes of ranvier from peripheral nerves of mice reconstructed by electron tomography. Neuroinformatics *3*, 133–162.

Steinhauser, M.L., Bailey, A.P., Senyo, S.E., Guillermier, C., Perlstein, T.S., Gould, A.P., Lee, R.T., and Lechene, C.P. (2012). Multi-isotope imaging mass spectrometry quantifies stem cell division and metabolism. Nature *481*, 516–519.

Su, J., Ekman, C., Oskolkov, N., Lahti, L., Ström, K., Brazma, A., Groop, L., Rung, J., and Hansson, O. (2015). A novel atlas of gene expression in human skeletal muscle reveals molecular changes associated with aging. Skelet. Muscle *5*, 35.

Tabb, D.L., McDonald, W.H., and Yates, J.R., 3rd. (2002). DTASelect and Contrast: tools for assembling and comparing protein identifications from shotgun proteomics. J. Proteome Res. *1*, 21–26.

Toyama, B.H., Arrojo E Drigo, R., Lev-Ram, V., Ramachandra, R., Deerinck, T.J., Lechene, C., Ellisman, M.H., and Hetzer, M.W. (2019). Visualization of long-lived proteins reveals age mosaicism within nuclei of postmitotic cells. J. Cell Biol. *218*, 433–444.

Toyama, B.H., and Hetzer, M.W. (2013). Protein homeostasis: live long, won't prosper. Nat. Rev. Mol. Cell Biol. *14*, 55–61.

Toyama, B.H., Savas, J.N., Park, S.K., Harris, M.S., Ingolia, N.T., Yates, J.R., 3rd, and Hetzer, M.W. (2013). Identification of long-lived proteins reveals exceptional stability of essential cellular structures. Cell *154*, 971–982.

Vazquez-Calvo, C., Suhm, T., Büttner, S., and Ott, M. (2020). The basic machineries for mitochondrial protein quality control. Mitochondrion *50*, 121–131.

Wirth, C., Brandt, U., Hunte, C., and Zickermann, V. (2016). Structure and function of mitochondrial complex I. Biochim. Biophys. Acta *1857*, 902–914.

Xu, T., Park, S.K., Venable, J.D., Wohlschlegel, J.A., Diedrich, J.K., Cociorva, D., Lu, B., Liao, L., Hewel, J., Han, X., et al. (2015). ProLuCID: an improved SEQUEST-like algorithm with enhanced sensitivity and specificity. J. Proteomics *129*, 16–24.

Yin, H., Price, F., and Rudnicki, M.A. (2013). Satellite cells and the muscle stem cell niche. Physiol. Rev. *93*, 23–67.

Zhang, D.S., Piazza, V., Perrin, B.J., Rzadzinska, A.K., Poczatek, J.C., Wang, M., Prosser, H.M., Ervasti, J.M., Corey, D.P., and Lechene, C.P. (2012). Multi-isotope imaging mass spectrometry reveals slow protein turnover in hair-cell stereocilia. Nature *481*, 520–524.

Please cite this article in press as: Krishna et al., Identification of long-lived proteins in the mitochondria reveals increased stability of the electron transport chain, Developmental Cell (2021), https://doi.org/10.1016/j.devcel.2021.10.008

CellPress

STAR★METHODS

KEY RESOURCES TABLE

REAGENT or RESOURCE	SOURCE	IDENTIFIER
Antibodies		
OxPhos Antibody Cocktail Rodent	Invitrogen	Cat#458099, RRID: AB_2533835
NDUFA9 Monoclonal Antibody	Invitrogen	Cat#459100, RRID: AB_2532223
UQCRC1 Monoclonal Antibody	Invitrogen	Cat#459140, RRID: AB_2532227
COX IV (3E11) Rabbit mAb	Cell Signaling	Cat#4850S, RRID: AB_2085424
COX7C Polyclonal Antibody	Invitrogen	Cat#PA551284 RRID: AB_2636731
NDUFA4 Polyclonal Antibody	Invitrogen	Cat#PA599439, RRID: AB_2818372
COX5A Polyclonal Antibody	Proteintech	Cat# 11448-1-AP, RRID: AB_2085429
α/β-Tubulin Antibody	Cell Signaling	Cat#2148S, RRID: AB_2288042
Myc-Tag (9B11) Mouse mAb	Cell Signaling	Cat# 2276S, RRID: AB_331783
Monoclonal ANTI-FLAG® M2 antibody	Sigma	Cat#F3165, RRID: AB_259529
Goat anti-Mouse IgG2a Cross-Adsorbed Secondary Antibody, Alexa Fluor 488	Invitrogen	Cat# A21131, RRID: AB_141618
Goat anti-Mouse IgG1 Cross-Adsorbed Secondary Antibody, Alexa Fluor 568	Invitrogen	Cat# A21124, RRID: AB_141611
Goat anti-Mouse IgG1 Cross-Adsorbed Secondary Antibody, Alexa Fluor 488	Invitrogen	Cat# A21121, RRID: AB_2535764
Goat anti-Mouse IgG2a Cross-Adsorbed Secondary Antibody, Alexa Fluor 568	Invitrogen	Cat# A21134, RRID: AB_1500825
Chemicals, peptides, and recombinant proteins		
^{15}N-spirulina algae	Cambridge isotope Laboratories	Cat#MF-SPIRULINA-N-S
2.5% Glutaraldehyde	Ted Pella Inc., Redding, CA	Cat#18426
2% Formaldehyde	Ted Pella Inc., Redding, CA	Cat#18200
Sodium Cacodylate	Ted Pella Inc., Redding, CA	Cat#18851
Osmium Tetroxide	Electron Microscopy Sciences	Cat#19190
Potassium Ferrocyanide	Electron Microscopy Sciences	Cat#3114
Thiocarbohydrazide	Electron Microscopy Sciences	Cat#21900
Durcupan ACM Resin	Sigma-Aldrich	Cat#44611 (Comp A), Cat# 44612 (Comp B), Cat#44613 (Comp C), Cat#44614 (Comp D).
Matrigel (Cultrex)	R&D Systems	Cat#3433-005-01
DMEM:F12 for SILAC	Fisher Scientific	Cat#88370
Dialyzed FBS	Gibco	Cat#26400044
DMEM for SILAC	Fisher Scientific	Cat#A33822
L-Lysine-$^{13}C_6$ hydrochloride	Sigma	Cat#643459
L-Arginine-$^{13}C_6$,$^{15}N_4$ hydrochloride	Sigma	Cat#608033
TCEP-HCL	Sigma-Aldrich	Cat#C4706
Chloroacetamide	Sigma-Aldrich	Cat#C0267
Trypsin	Promega	Cat# V5111
NativePAGE™ Sample Prep Kit	Invitrogen	Cat#BN2008
Native PAGE 3-12% gradient gel	Invitrogen	Cat# BN1001BOX
Dark Blue Cathode Buffer	Invitrogen	Cat# BN2002
Running Anode Buffer	Invitrogen	Cat#BN2001
Trizol	Invitrogen	Cat#15596026
SuperSignal West Pico	Fisher Scientific	Cat#PI34078
SYBR Green PCR Master Mix	Applied Biosystems	Cat#4309155
Ibidi u-Slide chambers	Ibidi	Cat#80826

(*Continued on next page*)

Please cite this article in press as: Krishna et al., Identification of long-lived proteins in the mitochondria reveals increased stability of the electron transport chain, Developmental Cell (2021), https://doi.org/10.1016/j.devcel.2021.10.008

Continued

REAGENT or RESOURCE	SOURCE	IDENTIFIER
4-hydroxytamoxifen (4OHT)	Sigma-Aldrich	Cat#H6278
Critical commercial assays		
RNeasy Mini Kit	Qiagen	Cat#74106
QuantiTect Reverse Transcriptase Kit	Qiagen	Cat#205311
Complex IV Rodent Enzyme Activity Microplate Assay Kit	Abcam	Cat# ab109911
Seahorse XF Cell Mito Stress Test	Agilent	Cat#103015-100
Seahorse XF Glycolysis Stress Test Kit	Agilent	Cat#103020-100
ATP Chemiluminescence Detection Assay Kit	Cayman Chemicals	Cat# NC1357058
L-Lactate Assay Kit	Abcam	Cat# ab65330
Deposited data		
Mass spectrometry Proteomic Datasets	ProteomeXchange Consortium via PRIDE (Perez-Riverol et al., 2019)	https://doi.org/10.6019/PXD028963
Experimental models: Cell lines		
SH-SY5Y	ATCC	Cat#CRL-2266
C2C12 Myoblasts	ATCC	Cat#CRL-1772
Human ES Cells (H9)	WiCell	Cat#WA09
Experimental models: Organisms/strains		
Mouse:FVB (Male)	The Jackson Laboratory, Bar Harbor,ME	Stock No: 001800
Oligonucleotides		
COX7C sh1 targeting sequence -TGCT GTTGACAGTGAGCGACCGCACCTTTC TTTATAGTAATAGTGAAGCCACAGAT GTATTACTATAAAGAAAGGTGCGGC TGCCTACTGCCTCGGA	This paper	Eton Biosciences; Sequences generated using shERWOOD algorithm (Knott et al., 2014)
COX7C sh2 targeting sequence - TGCT GTTGACAGTGAGCGCCACCAGCTACTT AAAAAATAATAGTGAAGCCACAGATGTA TTATTTTTTAAGTAGCTGGTGTTGCCTA CTGCCTCGGA	This paper	Eton Biosciences; Sequences generated using shERWOOD algorithm (Knott et al., 2014)
COX7C qPCR Primer: Forward - AGCATGTTGGGCCAGAGT	This paper	Eton Biosciences
COX7C qPCR Primer: Reverse- ACTGAAAACGGCAAATTCTT	This paper	Eton Biosciences
NDUFA4 qPCR Primer: Forward - CGCTTGGCACTGTTTAATCCA	This paper	Eton Biosciences
NDUFA4 qPCR Primer: Reverse - TCCATGGCTCTGGGTTGTTC	This paper	Eton Biosciences
COX5A qPCR Primer: Forward - CTGCCGCTGTCTGTTCCATTCG	This paper	Eton Biosciences
COX5A qPCR Primer: Reverse - TGTCACCCAGCGAGCATCAAACT	This paper	Eton Biosciences
Beta-actin qPCR Primer: Forward - CTGTCCCTGTATGCCTCTG	This paper	Eton Biosciences
Beta-actin qPCR Primer: Reverse - ATGTCACGCACGATTTCC	This paper	Eton Biosciences
Recombinant DNA		
UNG Construct	Addgene	Cat#127288
Plasmid: pRITE Myc to Flag (pRITE-MF)	(Toyama et al., 2019)	N/A
Plasmid: ATP5C1 RITE-MF pLentiCMVBlast	This paper	N/A

(*Continued on next page*)

Please cite this article in press as: Krishna et al., Identification of long-lived proteins in the mitochondria reveals increased stability of the electron transport chain, Developmental Cell (2021), https://doi.org/10.1016/j.devcel.2021.10.008

Continued

REAGENT or RESOURCE	SOURCE	IDENTIFIER
Plasmid: COX7C RITE-MF pLentiCMVBlast	This paper	N/A
shERWOOD UltramiR Lentiviral Inducible shRNA for NDUFA4	Transomic technologies	Cat#TLMSU2300-17992
Set of 3 SMARTvector Inducible Mouse COX5A (mCMV-TurboGFP shRNA) SMARTvector Inducible Lentiviral Control	Dharmacon	Cat#V3SM11256-01EG12858 Cat# VSC11651
Software and algorithms		
OpenMIMS	Steinhauser et al, 2012	https://github.com/BWHCNI/OpenMIMS/
Unwarp Plugin for ImageJ	Schneider et al., 2012; Sorzano et al., 2005	N/A
MesoFusion Plugin and Code for ImageJ	This paper; Mendeley Data	https://data.mendeley.com/datasets/b3hww8ng7w/1; https://doi.org/10.17632/b3hww8ng7w.1
Integrated Proteomics Pipeline Version 6.0.5 IP2	N/A	http://www.integratedproteomics.com/
Census2	Park et al., 2014	N/A
nl2sol algorithm	R package	http://www.netlib.org/port/
modelr algorithm	R package	https://CRAN.R-project.org/package=modelr
Proteomics Data Analysis Code (Mass spectrometry and half-life calculation)	This paper; Mendeley Data	https://data.mendeley.com/datasets/b3hww8ng7w/1; https://doi.org/10.17632/b3hww8ng7w.1
RCSB Protein Data Bank	https://www.rcsb.org/	mouse Complex I: 6G2J, human Complex III: 5XTE, human Complex IV: 5Z62, porcine respirasome: 5XTH
PyMOL	PyMOL by Schrödinger	https://pymol.org/2/
Half-life Color Code for PDB crystal structures in PyMOL	This paper; Mendeley Data	https://data.mendeley.com/datasets/b3hww8ng7w/1; https://doi.org/10.17632/b3hww8ng7w.1
Graphpad Prism 8.0	Graphpad	https://www.graphpad.com/scientific-software/prism/; RRID: SCR_002798

RESOURCE AVAILABILITY

Lead contact

All requests for further information, reagents and resources should be directed to the lead contact, Martin W. Hetzer (hetzer@salk.edu).

Materials availability

All materials generated in this study are available upon request to the lead contact.

Data and code availability

- All mass spectrometry proteomic datasets have been deposited to the ProteomeXchange Consortium via the PRIDE (Perez-Riverol et al., 2019) partner repository and are publicly available as of the date of publication. DOIs are listed in the key resources table.
- All original code has been deposited at Mendeley and is publicly available as of the date of publication. DOIs are listed in the key resources table.
- Any additional information required to reanalyze the data reported in this work paper is available from the lead contact upon request.

Please cite this article in press as: Krishna et al., Identification of long-lived proteins in the mitochondria reveals increased stability of the electron transport chain, Developmental Cell (2021), https://doi.org/10.1016/j.devcel.2021.10.008

EXPERIMENTAL MODEL AND SUBJECT DETAILS

Mouse

The mouse used in this study was of the FVB/NJ strain (Stock No: 001800), male and was acquired from the Jackson Laboratory (Maine, USA). The housing conditions used were 12/12h light-dark cycles, water and food provided *ad-libitum*. For the SILAM breeding, as described in the method details section, 6-week old FVB/NJ females (Jackson Laboratories) were fed *ad-libitum* with chow containing ^{15}N-spirulina algae (Cambridge isotope Laboratories, Inc.) for 70 days prior to mating with a male. Mating period was of 1 week. While female mice were used for the SILAM, the final MIMS-EM imaging study was conducted on 1 male mouse. All animal experimentation was approved by the University of California San Diego IACUC (protocol number S03172M).

Cell Culture

SH-SY5Y and C2C12 cells were all obtained from American Type Culture Collection (ATCC). SH-SY5Y cells were cultured in DMEM:F-12 with 10%FBS with Pen-Strep (growth media). For neuronal differentiation, SH-SY5Y cells were plated in growth media on ibidi chamber slides that had been previously coated with 10μg/ml polyornithine solution for 1 day, followed by 10μg/ml laminin for another day. The cells were grown until 80-90% confluent, then washed twice with PBS and switched to DMEM:F12 with 0.5%FBS, 3μM Retinoic Acid and Pen-Strep for 5 days to generate neurons as described previously (Cheung et al., 2009). Human ES H9 Cells (WiCell) cells with UNG construct (Addgene, 127288) were a kind gift from the Fred Gage lab. H9 cells were grown on Matrigel coated plates (R&D Systems, 3433-005-01) with iPS-Brew XF (Miltenyi Biotec, 130-104-368) for 24hours before induction with 2μg/ml Doxycycline (Sigma) for 3 days. For further maturation, induced neurons were switched to Neuronal Maturation Medium (NMM) containing 1:1 DMEM/F12 and Neurobasal Media, supplemented with GlutaMAX, B27, N2, 0.5mM dbcAMP, 20ng/ml GDNF and 20ng/ml BDNF, 10μg/ml laminin as well as 2μg/ml Doxycyline. At Day 7 cells were treated with 2μM AraC for 2 days to induce cell death of non-neuronal cells, following which cells were kept in the NMM till Day 11 to generate mature neurons as described previously (Schafer et al., 2019). C2C12 cells were cultured in DMEM with 20%FBS with Pen-Strep (growth media). For myotube differentiation, C2C12 cells were grown in growth media until fully confluent, then washed twice with PBS and switched to DMEM with 2% Horse Serum with Pen-Strep (differentiation media) for 5 days to generate mature myotubes as described previously (D'Angelo et al., 2009). All cells were cultured at 37°C with 5% CO_2, and media was changed every other day.

METHOD DETAILS

Stable isotope metabolic labelling of mammals (SILAM)

SILAM was performed as described previously (Arrojo et al., 2019). Briefly, 6-week old FVB/NJ females (Jackson Laboratories) were fed *ad-libitum* with chow containing ^{15}N-spirulina algae (Cambridge isotope Laboratories, Inc.) for 70 days prior to mating with a male. Mating period was of 1 week. ^{15}N-chow was provided throughout the mating period as well as gestation and lactation period until the ^{15}N-labelled pups were 21 days (P21) in post-natal age. Pups were weaned at P21 and fed ^{15}N-chow until they were P45, after which their food source was replaced with ^{14}N-chow. The pups were then euthanized, perfused with fixative as previously described (Sosinsky et al., 2005) at 6-months after the start of feeding with ^{14}N-chow. The perfusion process was as follows: mice were anesthetized with a ketamine:xylazine mix and transcardially perfused with a solution of 2.5% glutaraldehyde, 2% PFA in 0.15M sodium cacodylate buffer containing 2mM calcium chloride warmed to 37°C. Perfusion time was of 10 minutes and the brain and skeletal muscle depots were dissected, the brain was further cut into 150-micron thick slices with a vibratome (Leica VT100S), and both tissue types prepared for electron microscopy.

Sample processing for Scanning Electron Microscopy imaging

After dissection and sectioning, the samples were post-fixed in the same fixative at 4°C overnight. The brain slices were washed with cacodylate buffer and then fixed in a solution containing 2% osmium tetroxide, 1.5% potassium ferrocyanide in cacodylate buffer for 1 hour at room temp (25°C). Samples were washed with water and placed in a solution of 0.5% thiocarbohydrazide for 30 minutes and washed with water. Next, samples were placed in 2% aq. osmium tetroxide for 1 hour, washed with water and then placed in 2% aq. uranyl acetate at 4°C overnight. Samples were again washed with water and placed into Walton's lead aspartate solution for 30 min at 60°C, followed by washes in water and sequential dehydration with 70% EtOH, 90% EtOH, 100% EtOH, 100% EtOH, and dry acetone (10 minutes each step) on ice. Next, the samples were placed into 1:3, 1:1, and 3:1 solutions of Durcupan ACM:acetone for 12 hours each. Lastly, the samples were placed into 3 changes of 100% Durcupan ACM for 1 day each and baked at 60°C for 48 hours and stored in aluminum foil dishes until sectioning in 80nm-thick sections using an ultra-microtome (Leica).

Multi-isotope mass spectroscopy and scanning electron microscopy

Correlated Multiple isotope mass spectrometry imaging (MIMS) and scanning electron microscopy imaging (called MIMS-EM) was used to quantify the concentration of ^{15}N and ^{14}N in brain tissue sections from ^{15}N-labelled mice in this study. First, 80nm-thick sections of ^{15}N-labelled brain and intercostal muscle (ICM) from animals chased for 6-months were placed on a 5x7mm Si wafer (TedPella). Next, we used the Atlas 5 engine (Fibics, Ottawa, Canada) to create large field of view maps with 5nm pixels in X-Y of sections of the mouse cerebellum and ICM using scanning electron microscopy (GeminiSEM, MerlinSEM (Zeiss, Germany). We targeted the granular cell layer in the cerebellum and the neuromuscular junction region in the ICM. MIMS image acquisition of mapped

Please cite this article in press as: Krishna et al., Identification of long-lived proteins in the mitochondria reveals increased stability of the electron transport chain, Developmental Cell (2021), https://doi.org/10.1016/j.devcel.2021.10.008

regions of interest was done as previously described (Arrojo et al., 2019; Steinhauser et al., 2012; Zhang et al., 2012). Here, sections of cerebellum and ICM tissue sections containing mapped cells and organelles were imaged with a NanoSIMS 50L (Cameca, France) using a cesium (Cs-) beam, 1024x1024 image raster and ^{15}N and ^{14}N levels were detected simultaneously.

Stable isotope labeling by amino acids in cell culture (SILAC)

For the H9 ES cell SILAC, light media was regular DMEM:F12 supplemented with GlutaMAX, B27, N2, 0.5mM dbcAMP, 20ng/ml GDNF and 20ng/ml BDNF, 10μg/ml laminin and 2μg/ml Doxycyline. Heavy media was DMEM:F12 for SILAC (Fisher Scientific, 88370) with heavy amino acids L-Lysine-$^{13}C_6$ hydrochloride (Sigma, 643459) and L-Arginine-$^{13}C_6$,$^{15}N_4$ hydrochloride (Sigma, 608033), also supplemented with above mentioned factors. For the SILAC timecourse, H9 cells were differentiated into neurons for 11 days as mentioned before, and this day was treated as the beginning of the timecourse (Day 0). Neurons were switched to heavy media for the Day 8 timepoint and light media for the other timepoints on this day. The media was switched to heavy for the other timepoints on respective days and the neurons for all timepoints were harvested 8 days after the beginning of the timecourse. Media was refreshed every other day. For the C2C12 SILAC, light media was regular DMEM with 2% Dialyzed FBS (Gibco, 26400044) with Pen-Strep, and heavy media was DMEM for SILAC (Fisher Scientific, A33822) with 2% Dialyzed FBS with Pen-Strep and heavy amino acids L-Lysine-$^{13}C_6$ hydrochloride and L-Arginine-$^{13}C_6$,$^{15}N_4$ hydrochloride. For the SILAC timecourse, C2C12 cells were differentiated for 5 days in differentiation media, and this day was treated as the beginning of the timecourse (Day 0). The rest of the timecourse was conducted exactly like the neuronal SILAC mentioned before.

Fractionation and LC/MS Analysis

Neurons were harvested at the end of the SILAC timecourse by washing the plate with 1xPBS and spinning down the pellet at 1200rpm for 5min. They were then fractionated into crude nuclear, mitochondrial and cytosolic fractions as described previously (Clayton and Shadel, 2014). Briefly, neuronal cell pellets were resuspended in Mannitol-Sucrose (MS) Buffer (210mM Mannitol, 70mM Sucrose, 5mM Tris HCL pH 7.5, 5mM EDTA pH 8 and protease inhibitors), followed by mechanical lysis through a $27_{1/2}$-gauge needle and syringe. The homogenate was centrifuged at 1000g for 5min for crude nuclear pellet, and the supernatant was centrifuged at 10,000g for 20min to get the crude mitochondrial pellet. The remaining supernatant was kept as the cytosolic fraction. Myotubes were harvested at the end of the SILAC timecourse through selective trypsinization for 5mins to separate them from the mononuclear reserve cell population. The harvested myotubes were either kept as whole cell pellets or fractionated into crude nuclear and mitochondrial pellets only. The different fractions for neurons (nuclear, mitochondria and cytosolic) and myotubes (whole cell, nuclear and mitochondrial) were precipitated by methanol/ chloroform and redissolved in 8M urea/100mM TEAB, pH 8.5. Proteins were reduced with 5 mM tris(2-carboxyethyl) phosphine hydrochloride (TCEP-HCL, Sigma-Aldrich, C4706) and alkylated with 10 mM chloroacetamide (Sigma-Aldrich, C0267). Proteins were digested overnight at 37°C in 2M urea/100mM TEAB, pH 8.5, with trypsin (Promega, V5111) and digestion was quenched with formic acid at 5% final concentration. The samples were then subject to electrospray ionization (ESI) and tandem mass spectrometry (MS/MS), to identify peptides and determine their heavy to light ($^{13}C_6$/$^{12}C_6$ and $^{15}N_4$/$^{14}N_4$) isotope ratios as described previously (Buchwalter et al., 2019). Briefly, digested samples were run with CID fragmentation on a Thermo Orbitrap Fusion Lumos Tribrid MS/MS by direct injection onto a column (30cm, 75uM ID column with BEH 1.7um C18 resin). A flow rate of 300nl/min was used on a nLC 1200 for separation of the injected samples. 0.1% formic acid (water) was used as Buffer A and 0.1% formic acid (90% acetonitrile) was used as Buffer B. A total run time of 240 minutes was used, with the first 180 minutes run on a gradient of 1-25% B, the next 40 minutes was an increase to 50% B, the next 10 minutes was an increase to 100% B and the final 10 minutes was held at 100%B. Before sample injection, re-equilibration of the column was performed with Buffer A and peptide elution was conducted directly from the column tip. By using 2.8 kV voltage at the back of the column, the eluted peptides were then nanosprayed into the mass spectrometer. The Lumos MS/MS was operated in data dependent mode and the collection of full MS1 scans was performed in the Orbitrap. The data collection was conducted with a resolution of 120K, a mass range of 400-1500 m/z and a target of $4e^5$ for the AGC. For each scan, the most abundant ions were selected for CID MS/MS within a cycle time of 3s. An AGC target of $4e^5$ and minimum intensity of 5000 was used in the ion trap. A maximum fill time of 50ms was used for the MS scans and 100ms for the MS/MS scans. Monoisotropic precursor selection was allowed and a quadruple isolation of 1.6 m/z was used. 2-7 charge states were chosen and a 5s exclusion duration was used with dynamic exclusion.

BN-PAGE and western blots

Blue-native PAGE gels were conducted as described previously (Jha et al., 2016). Briefly, crude mitochondria were isolated as mentioned in the previous section from dividing myoblasts and differentiated myotubes, or for control and COX7C-knockdowns for differentiating myotubes, Day 8,16 and 24 myotubes. The mitochondrial pellets were subject to digitonin solubilization at 8g/g digitonin/protein ratio using NativePAGE™ Sample Prep Kit (Invitrogen, BN2008). For BN-PAGE gels subject to Coomassie staining (for dividing myoblasts, myotubes, and the SILAC samples) 100μg mitochondrial pellet protein was used for each sample to clearly visualize the supercomplex and individual complex bands. For the BN-PAGE that was transferred onto a membrane for western blots 50ug mitochondrial pellet protein was used for each sample. Upon addition of digitonin, the mitochondria were put on ice for 20min. The solubilized mitochondria were then centrifuged at 20,000g for 10 mins at 4°C, and the supernatant collected. Coomassie G-250 was added to the supernatant at a 1:7.5 ratio (2μl G-250/15μl supernatant) before loading the samples in a Native PAGE 3-12% gradient gel (Invitrogen, BN1001BOX) with dark blue cathode buffer (Invitrogen, BN2002) in the inner chamber and running anode buffer (Invitrogen, BN2001) in the outer chamber. The gel was run for 30 minutes at 150V, after which the dark blue cathode buffer

in the inner chamber was replaced with running anode buffer and run for another 60 minutes at 250V. The gel was either stained with Coomassie and destained for BN-PAGE or transferred onto PVDF membrane. Post-transfer the PVDF membrane was destained with 100% methanol before blocking and adding primary antibodies against Oxphos Cocktail (Invitrogen, 458099), Complex I subunit NDUFA9 (Invitrogen, 459100), Complex III subunit UQCRC1 (Invitrogen, 459140) and Complex IV subunit COXIV (Cell Signaling, 4850S) at 1:1000 dilution in 5% BSA/TBST overnight at 4 degrees. Blots were washed 3x in TBST and incubated with HRP-conjugated secondary antibodies for 1 hour, and developed using SuperSignal West Pico (Thermo Scientific, PI34078).

Gel Band Extraction and LC/MS Analysis

The SILAC samples from Day 0-8 were all subject to mitochondrial fractionation and digitonin solubilization and run on BN-PAGE gels as described above. The gels were stained in Coomassie and destained, and the bands on the gels were cut as labelled in Figure 3A and put in tubes as follows: Sample 1 – SCI,III_n,IV_n, Sample 2 – SCIII_2,IV, Sample 3 – CIII_2,CIV_2, Sample 4 – CI and CII, Sample 5 – CIV. Each tube containing the gels was destained with 50% methanol/5% acetic acid overnight and dehydrated with 100% acetonitrile (ACN) twice. The gels were air dried, then 5mM TCEP-HCl was added for 30mins and removed, followed by treatment with 50mM chloroacetamide for 30 mins in the dark. The chloroacetamide was removed, and the gels washed twice in ACN, and dried. 20ng/ul trypsin (Promega, V5111) in 100mM ammonium bicarbonate was then added to barely cover the gels and incubated overnight. The gels were then incubated with 5% formic acid (without removing the liquid from the tube) for 10 mins, and the supernatant stored in a new tube. The gels were incubated with 50% ACN/5% formic acid twice and the supernatant stored in the same tube. The eluate was then dried down, and peptides were resuspended in Buffer A (0.1% formic acid in water). The digested samples were then run on a Thermo Orbitrap Fusion Tribrid MS/MS with a flow rate of 200nl/min on a nLC 1000. The rest of the LC/MS was conducted following the same protocol as described above for the fractionated and whole cell samples.

shRNA construction, lentiviral generation and knockdowns

shRNA's targeting mouse COX7C were designed using the shERWOOD algorithm (Knott et al., 2014), with sequences listed in the key resources table. The shRNA's were cloned into the miR-E lentiviral plasmid LT3GEPIR (Fellmann et al., 2013) using EcoRI and XhoI restriction sites for doxycycline-inducible knockdowns. The shRNA's targeting mouse NDUFA4 and COX5A were purchased from Transomic technologies (shERWOOD UltramiR Lentiviral Inducible shRNA, Cat#TLMSU2300-17992) and Dharmacon (SMARTvector Inducible Lentiviral shRNA, Cat#V3SM11256-01EG12858) respectively. 293T cells were transfected with 3rd generation packaging plasmids and the control or knockdown lentiviral plasmids, and virus was collected at 48 and 72 hours. C2C12 cells were transduced with virus diluted 1:1 with growth media containing 6ug/mL polybrene for 24 hours and selected with 5ug/ml puromycin for 48-72 hours to generated stable cell lines. For knockdowns in dividing myoblasts C2C12 control, sh1 and sh2 lines were exposed to doxycycline for 4 days. For differentiating myotubes, dividing cells were exposed to dox for 4 days and then switched to differentiation media with dox for 5 days. For differentiated myotubes, cells were differentiated into myotubes first (as described before) and then exposed to dox for 8,16 and 24 days. In all conditions, media was changed every other day. At the end of the timepoints, myoblasts or myotubes were harvested using trypsinization and subject to qPCR and western blots.

qPCR

Control and COX7C-knockdowns in myoblasts and myotubes were homogenized in Trizol (Invitrogen, 15596026) and total RNA extracted using RNeasy Mini Kit (Qiagen, 74106). 1ug of RNA was then reverse transcribed into cDNA using the QuantiTect Reverse Transcriptase Kit (Qiagen, 205311). The cDNA samples were diluted 1:10 and qPCR performed with SYBR Green PCR Master Mix (Applied Biosystems, 4309155) and primers against mouse COX7C, NDUFA4, COX5A and beta-Actin using the Bio- Rad iCycler real-time system. qPCR primers used are listed in the key resources table.

Western Blotting

Control and COX7C-knockdowns in myoblasts and myotubes were lysed by boiling the samples in SDS lysis buffer (4% SDS, 100mM Tris pH 6.8) for 10 minutes. Lysates were quantified using BCA protein assay, and loaded on 10% gels, transferred on nitrocellulose membrane (Protran NC, GE Healthcare Biosciences), blocked with 5% BSA/TBST and incubated with anti-COX7C (Invitrogen, PA551284), NDUFA4 (Invitrogen, PA599439), COX5A (Proteintech, 11448-1-AP) and Tubulin (Cell Signaling, 2148S) primary antibodies at 1:1000 dilution in 5% BSA/TBST overnight at 4 degrees. Blots were washed 3x in TBST and incubated with HRP-conjugated secondary antibodies for 1 hour, and developed using SuperSignal West Pico (Thermo Scientific, PI34078).

RITE plasmid generation, tag switching and immunofluorescence

pRITE Myc to Flag (pRITE-MF) construct was generated previously (Toyama et al., 2019). Human ATP5C1 ORF sequence or Mouse COX7C ORF sequence was cloned into the pRITE-MF constructs using NheI and XhoI restriction sites. The ATP5C1 and COX7C RITE-MF constructs were then amplified using degenerate gateway primers, which were then cloned into pDONR207 constructs using Gateway cloning BP reaction (ThermoFisher). The ATP5C1 and COX7C RITE-MF pDONR207 gateway constructs were then recombined into lentiviral vector pLentiCMVBlast (http://www.ericcampeau.com) using the LR reaction (Gateway Cloning, ThermoFisher). 293T cells were transfected with 3rd generation packaging plasmids and the ATP5C1 and COX7C RITE-MF pLentiCMVBlast plasmid and virus was collected at 48 and 72 hours. SHSY-5Y and C2C12's were transduced with the ATP5C1

Please cite this article in press as: Krishna et al., Identification of long-lived proteins in the mitochondria reveals increased stability of the electron transport chain, Developmental Cell (2021), https://doi.org/10.1016/j.devcel.2021.10.008

RITE-MF and COX7C RITE-MF viruses respectively at a dilution of 1:1 with growth media containing 6ug/mL polybrene for 24 hours, and selected with 10ug/ml blasticidin for 48-72 hours to generated stable cell lines. Full sequences are available upon request.

ATP5C1 RITE-MF SHSY-5Y cells were plated on Polyornithine and Laminin coated ibidi u-Slide chambers and differentiated into neurons as described before. Tag exchange was initiated by adding concentrated adenovirus expressing Cre (Ad-Cre) to the media. Media was changed for cells every other day, and cells were fixed 6 days after Ad-Cre exposure.

COX7C RITE-MF C2C12 dividing myoblasts were plated on ibidi u-Slide chambers (80826, Ibidi), and tag exchange was initiated by adding concentrated adenovirus expressing Cre (Ad-Cre) to the media. Media was changed for cells every other day, and cells were fixed 4 days after Ad-Cre exposure. For RITE exchange in myotubes, COX7C RITE-MF myoblasts were plated with Cre-expressing CreER2 C2C12 cell line in a 5:1 ratio on ibidi slides as described previously (Toyama et al., 2019). When the cells were fully confluent, differentiation media was added for 5 days to generate myotubes. Tag exchange was initiated by addition of 1uM of 4-hydroxytamoxifen (4OHT) (H6278, Sigma) 4 or 8 days before fixation for Day 4 and Day 8 timepoints respectively. Media was changed every other day. At the final timepoints for SHSY-5Y neurons, COX7C dividing cells and myotubes, the entire slide (all timepoints) was fixed with 4% paraformaldehyde (Electron Microscopy Sciences) for 5mins, and blocked in IF buffer (0.1% Triton X-100, 0.02% SDS, 20mg/mL BSA, in PBS) for 20 mins at room temperature (RT). The slide was then stained for anti-Myc (9B11, Cell Signaling) and anti-Flag (M2, Sigma) antibodies for 2 hours at 1:1000 dilution in IF buffer at RT. The slides were washed 3x in PBS, and secondary antibodies anti-mouse IgG2a-488 (A21131, Invitrogen) and anti-mouse IgG1-568 (A21124, Invitrogen) for SHSY-5Y cells and anti-mouse IgG1-488 (A21121, Invitrogen) and anti-mouse IgG2a-568 (A21134, Invitrogen) for C2C12 cells were added at 1:1000 dilution in IF buffer at RT in the dark. The slides were washed 3x in PBS and Hoechst dye was added to stain the nuclei. The slides were imaged using confocal microscopy on a Leica SP8.

Mitochondrial functional assays

Complex IV Assay was performed using the Complex IV Rodent Enzyme Activity Microplate Assay Kit (Abcam, ab109911). Briefly, control and COX7C-knockdowns in myotubes were fractionated for mitochondria as described before. The mitochondrial pellets were digitonin-permeabilized as described before, and the supernatant loaded on the 96-well microplate from the kit for 3h at RT. The wells were washed, and the substrate reduced cytochrome c was added to the wells before measuring the absorbance at 550nm at 30°C for 120 minutes. The data was quantified by plotting the absorbance over time, fitting a line through the curve and measuring the slope, which was normalized to the controls. Mitochondrial respiration was measured using the Seahorse XFe96 Assay and Analyzer (Agilent). Briefly, control and COX7-knockdowns in differentiating myotubes grown in 96-well Seahorse XF Cell Culture Microplate and the Seahorse XF Cell Mito Stress Test for OCR, (Agilent, 103015-100) and the Seahorse XF Glycolysis Stress Test Kit for ECAR, (Agilent, 103020-100) were conducted using the manufacturer's protocol. OCR was conducted using the following injections: 1) Oligomycin 2μM, 2) FCCP 2μM 3) Rotenone 2μM + Antimycin-A 2μM, while ECAR was conducted with 1) Glucose 10μM 2) Oligomycin 2μM 3) 2-DG 50μM. ATP Levels were measured using a luminescence ATP Detection Assay Kit (Cayman Chemicals, NC1357058). Briefly, control and COX7C-knockdowns in differentiating myotubes were homogenized in ATP sample buffer and loaded on a 96-well microplate along with the standards. The reaction mix containing D-luciferin and Luciferase in the ATP assay buffer was added to samples and standards, and the plate was incubated for 15mins at RT in the dark. The luminescence was then measured using a plate reader, the ATP concentration in samples determined using the standard curve, and the values were normalized to protein concentration for each sample. Lactate Assays was performed using the L-Lactate Assay Kit (Abcam, ab65330). Briefly, cell culture medium from control and COX7C-knockdowns was diluted 1:500 with Lactate Assay buffer and loaded on a 96-well microplate along with L-Lactate standards. The reaction mix containing the probe and enzyme was then added to the plate and incubated for 30mins at RT in the dark. The lactate levels were then measured using a plate reader at absorbance of 570nm, the lactate concentration in samples determined using the standard curve, and the values were normalized to protein concentration for each sample.

QUANTIFICATION AND STATISTICAL ANALYSIS

MIMS image analysis, alignment and quantification

With MIMS-EM, the correlation and overlay of $^{15}N/^{14}N$ ratio images atop SEM micrographs has the advantage of displaying the chemical information of the sample while retaining the resolution and ultrastructural detail afforded by the SEM. An SEM image on UCSD's Zeiss platform can be acquired for a raster size of up to 32k X 32k pixels. In comparison, the raster size on Caltech's Cameca NanoSIMS can go up to a maximum of only 1024 X 1024 pixels. Beyond differences in scale, the signal collection mechanisms for the two instruments are completely different. When imaging sections in the SEM (to be later interrogated by nano-SIMS), signal collection is non-destructive, while in the NanoSIMS the signals are collected destructively by the sputtering atoms from the sample (Benninghoven et al., 1987). The sputter rates are vastly different for the different atomic species, resulting in a non-linear distortion of the NanoSIMS image with respect to the SEM ultrastructural reference image, complicating the fusion of these datasets. Manual alignment of the two images can insert operator bias into the correlation process. Automated alignment using simple affine transformations is also insufficient given the non-linear nature of the distortions. For proper alignment, the $^{15}N/^{14}N$ ratio image needs to be automatically adjusted for warping with respect to the SEM image. There are freely available warp adjustment softwares, such as the 'UnwarpJ' plugin of ImageJ (Schneider et al., 2012; Sorzano et al., 2005) that adjusts for distortions in one image with respect to the undistorted image. However, the plugin expects that the images be somewhat similar i.e. they are from the same imaging modalities.

Please cite this article in press as: Krishna et al., Identification of long-lived proteins in the mitochondria reveals increased stability of the electron transport chain, Developmental Cell (2021), https://doi.org/10.1016/j.devcel.2021.10.008

To facilitate the seamless alignment of the MIMS image to the SEM image, we developed a plugin called 'MesoFusion', which stands for Mesoscale Image Fusion. The plugin has 4 subroutines: 1. Rescale and Resize 2. Create Layout 3. Categorize Ratio map 4. Colorize Ratio map, the utility of each of the sub-routine will be shown with the aid of the Figure S1A. The Figure S1Aa, shows the SEM image (6500 X 7000 pixels) of cerebellar granule neurons from a 6-month chase mouse, acquired at a pixel size of 400nm. Figure S1Ab, shows the N15/N14 ratio map (512 X 512 pixels) of the same region, acquired at a pixel size of 400nm. It is clearly evident that at a macro level, these two images differ markedly in detail, scale, orientation and field of view (FOV). The Rescale and Resize subroutine, up-scales the MIMS image to match the pixel size of the SEM image, and roughly aligns both the images for any linear shifts, orientation and image flip. It also matches the two images such that they have roughly the same FOV, see Figures S1Ac and S1Ad. The subroutine Create Layout applies appropriate threshold and skeletonizes these two images so as to convert them to somewhat similar looking images, as shown in Figures S1Ae and S1Af. Now these two images can be fed into already available warping programs like UnwarpJ (Sorzano et al., 2005), and compensated for any shrinkage and distortion. Figures S1Ag and S1Ah, show the macro and micro distortion map, when the skeletonized MIMS image (Figure S1Af) was adjusted to the skeletonized SEM image (Figure S1Ae) using UnwarpJ. The transformations can be saved and applied to the originally aligned MIMS image prior to skeletonization (Figure S1Ad). The subroutine Categorize Ratio map divides the completely aligned $^{15}N/^{14}N$ ratio map into different categories based on the signal intensity i.e. concentration of the N15 signal with respect to the natural ratio. The Figures S1Ai, S1Aj, S1Ak, and S1Al, show the $^{15}N/^{14}N$ ratio map categorized into 2-3, 3-7, 7-50 and > 50 times the natural ratio. Finally, these four images are colorized and overlaid over the conventional SEM image, by the Colorize Ratio map subroutine as shown in Figure S1Am. The algorithm used in Colorize Ratio map has been described in detail elsewhere (Adams et al., 2016), but new features have been added to accommodate color schemes for people with color vision deficiencies (Keene, 2015). The MesoFusion plugin will be made available to the scientific community at no cost and can be requested from the authors. For quantification of the $^{15}N/^{14}N$ signal, the raw ratio was calculated by manually drawing around individual mitochondria, and similarly sized circles in the lumen and cytosol in the final aligned $^{15}N/^{14}N$ image. The raw values were then divided by $37x10^{-4}$ to determine the $^{15}N/^{14}N$ fold over natural ratio. This plugin along with an instruction manual is available online (Mendeley Data https://doi.org/10.17632/b3hww8ng7w.1).

Mass spectrometry data analysis and peptide filtration

Post-mass spectrometry, the identification, quantification and preliminary analysis of the peptides and proteins was performed on the Integrated Proteomics Pipeline Version 6.0.5 IP2 (http://www.integratedproteomics.com/). The tandem mass spectra were extracted using RawConverter from raw files (He et al., 2015) and searched against a nonredundant mouse UniProt database using ProLUCID (Xu et al., 2015). The search space included all fully-tryptic and half-tryptic peptide candidates, and cysteine-specific static modification of 57 was allowed for carbamidomethylation. SILAC labeling at K (6.0201) and R (10.0083) were searched as heavy metabolic labeling. A high-resolution precursor/peptide mass tolerance of 50ppm was used with the precursor mass range from 600 to 6000ppm. DTASelect software (Tabb et al., 2002) was used to filter the identified proteins which were searched against a target-decoy database to keep the false discovery rate to 1% at the protein level (Peng et al., 2003). A minimum of 1 peptide per protein and 1 tryptic end per peptide was required. A false positive rate of 0.01 and precursor delta mass cutoff of 10ppm was used to filter the data.

Quantification of SILAC-labeled peptides was performed using the software Census2 (Park et al., 2014). The peptides were further filtered based on rigorous quality control criteria of a minimum profile score of 0.8, and peptides with area ratios from 0.111-9 were required to have a minimum regression score of 0.8. Peptides with extreme area ratios <0.111 or >9 were only retained if the regression score was >0. The percent heavy label (percent new protein) was then calculated by transforming the area ratio values using the following equation:

$$\%\ heavy = 100 * (1 / (1 + Area\ Ratio))$$

$$\%\ light\ (\%\ old\ protein) = 100 - \%\ heavy$$

The mean, median, standard deviation and interquartile range was calculated for each peptide and outlier peptides were removed if they fell outside 20 times the interquartile range. The mass spectrometry proteomics data have been deposited to the ProteomeXchange Consortium via the PRIDE partner repository with the dataset identifier PXD028963 and https://doi.org/10.6019/PXD028963.

Half-life calculation

The individual peptide data for each protein was then pooled together and we restricted our analysis to proteins that had at least 2 peptides detected at 3 different timepoints during the timecourse. To assess protein turnover, we used the following exponential plateau decay equation, $y(t) = y_f + (y_0 - y_f)\, e^{-\alpha t}$, where: y = % light at time t, α = rate of turnover, y_f = minimum value of % light, y_0 = starting value of % light. To estimate the parameters of this nonlinear model, we used nonlinear least-squares (NLS) regression via the nls function in R with the nl2sol algorithm from the Port library (http://www.netlib.org/port/) . For very long-lived proteins, like histones, that barely show any turnover during the SILAC timecourse, the available data does not encompass enough timepoints to allow for an accurate fit of an exponential decay curve within this timeframe. Hence, in these cases, an alternate linear model was

Please cite this article in press as: Krishna et al., Identification of long-lived proteins in the mitochondria reveals increased stability of the electron transport chain, Developmental Cell (2021), https://doi.org/10.1016/j.devcel.2021.10.008

used to estimate the turnover rate α, as follows: $\log(y) = \beta + \alpha t$, where β = intercept and other parameters as described above. To assess model quality, the value of R-square was calculated for all models using the rsquare function from the modelr package in R (https://CRAN.R-project.org/package=modelr) and estimates were filtered for R-square values above 0.9. The estimated rate of turnover (α), was then used to calculate protein half-life with the following formula, $T_{half} = \ln(2)/-\alpha$. For neurons, the linear and port model showed very similar results, hence the port model was chosen to maintain consistency for comparisons of half-lives of mitochondrial proteins with myotubes.

For neurons, the data from nuclear, mitochondrial and cytosolic fractions was pooled together in order to improve the coverage of proteins. The pooled data was then separated based on human databases of different organelles (Nucleus, Mitochondria, ER, Lysosome, Cytosol) and submitochondrial compartments (Outer Mitochondrial Membrane, Inner Mitochondrial Membrane, Intermitochondrial Membrane Space, Nucleoid, Matrix) downloaded from Uniprot. For myotubes, the whole cell pellet, nuclear and mitochondrial fractions the replicates were analyzed separately, and the whole cell data was separated into different organelles using mouse Uniprot databases. Nuclear and mitochondrial proteins were taken from their respective fractions for most of the analysis as they had sufficient coverage (They showed similar data to nuclear and mitochondrial proteins from whole cell data). ETC proteins were collated by hand for both human and mouse. For both neurons and myotubes, 3 independent biological replicates were performed, and the average %old protein and median half-life values across the 3 replicates shown for the graphs. However, for gel bands, in order to increase coverage of the ETC proteins, the 3 individual replicate experiments were pooled at the peptide level after calculating the % heavy label. Outlier peptide removal was then performed using the interquartile range and the remaining analysis of half-life values was done similarly. We used half-lives that were ~2-fold higher than the respective average whole cell fractions as the cut-off value for a mitoLLP (>8.5 days in neurons and > 6 days in myotubes). These mass spectrometry data sets and the Uniprot databases used are available in Tables S1 and S2. The computer code developed in this paper for analyzing SILAC mass spectrometry datasets generated after Census2 and calculating half-lives is available online (Mendeley Data https://doi.org/10.17632/b3hww8ng7w.1).

NSAF analysis

NSAF values for all the proteins in the Day 0 timepoint of 5 samples of higher-order SCs (SCI,III,IV), intermediate SC (SCIII,IV), dimers (III_2,IV_2), individual CI & CII pooled (CI,II) and individual CIV (CIV) were calculated using the ID Compare function on IP2. NSAF values of proteins in CI, CII, CIII and CIV were then subset and summed up to calculate the total NSAF value for each complex. The NSAF values of each complex was then divided by the total NSAF for all the four complexes CI-CIV and multiplied by 100 to generate % NSAF values for each complex in each gel band sample.

Half-life visualization of crystal structures

In order to color code the crystal structures of proteins in complexes with their respective half-lives, the structure of the complex of interest was downloaded from RCSB Protein Data Bank (https://www.rcsb.org/). The accession code for the complexes were as follows - mouse Complex I: 6G2J, human Complex III: 5XTE, human Complex IV: 5Z62, porcine respirasome: 5XTH. (Human CIII and CIV, and porcine respirasome structures were used as mouse structures are not available). Using a script, the downloaded structures were color-coded with half-lives ranging from 2 days to 8 days, from dark red to white to dark blue for regular turnover rates. For the differential turnover between supercomplexes and individual complexes, the subtracted half-lives ranged from -1 to +1 days, from dark red to white to dark blue. The subunits without any coverage in the mass spectrometry and half-life data were labelled grey. The computer code developed in this paper for downloading the PDB crystal structure file into Pymol and color coding the crystal structures with half-lives is available online (Mendeley Data https://doi.org/10.17632/b3hww8ng7w.1).

RITE & Myotube Image Analysis

The RITE images for SHSY-5Y and COX7C were quantified using ImageJ (with FIJI). Each image was set to maximum projection and average intensity, and an outline was drawn manually around the cells, followed by measurement of the area, mean intensity and integrated density of the green and red channels using the measure function of ImageJ. Outlines were also drawn to take a background signal reading for each image. For quantification the background signal was subtracted from the cell signal to generate the total fluorescent intensity for the red and green channels. For ratio measurements the green to red intensities were divided, whereas for %old protein the individual channel intensity was divided by the total intensity (green+red) for each cell. Myotube thickness was measured by drawing lines across each myotube every 1 inch and then measuring the pixel length. The values for all myotubes in images were averaged and compared between control and knockdowns.

Statistical methods and representative figures

Error bars show mean ± SD from n=3 replicates for all graphs except when indicated. For MIMS-EM images, data are from 1 mouse and error bars show mean ± SD of N^{15}/N^{14} ratio for multiple mitochondria and other regions in the images shown. p-Values were obtained using an unpaired two-tailed Student's t test. All correlation coefficients represent Spearman's coefficient. Graphpad prism was used to conduct statistical analysis and make graphs. Images and western blots are representatives of at least 3 independent experiments unless otherwise stated.

Developmental Cell, Volume *56*

Supplemental information

Identification of long-lived proteins in the mitochondria reveals increased stability of the electron transport chain

Shefali Krishna, Rafael Arrojo e Drigo, Juliana S. Capitanio, Ranjan Ramachandra, Mark Ellisman, and Martin W. Hetzer

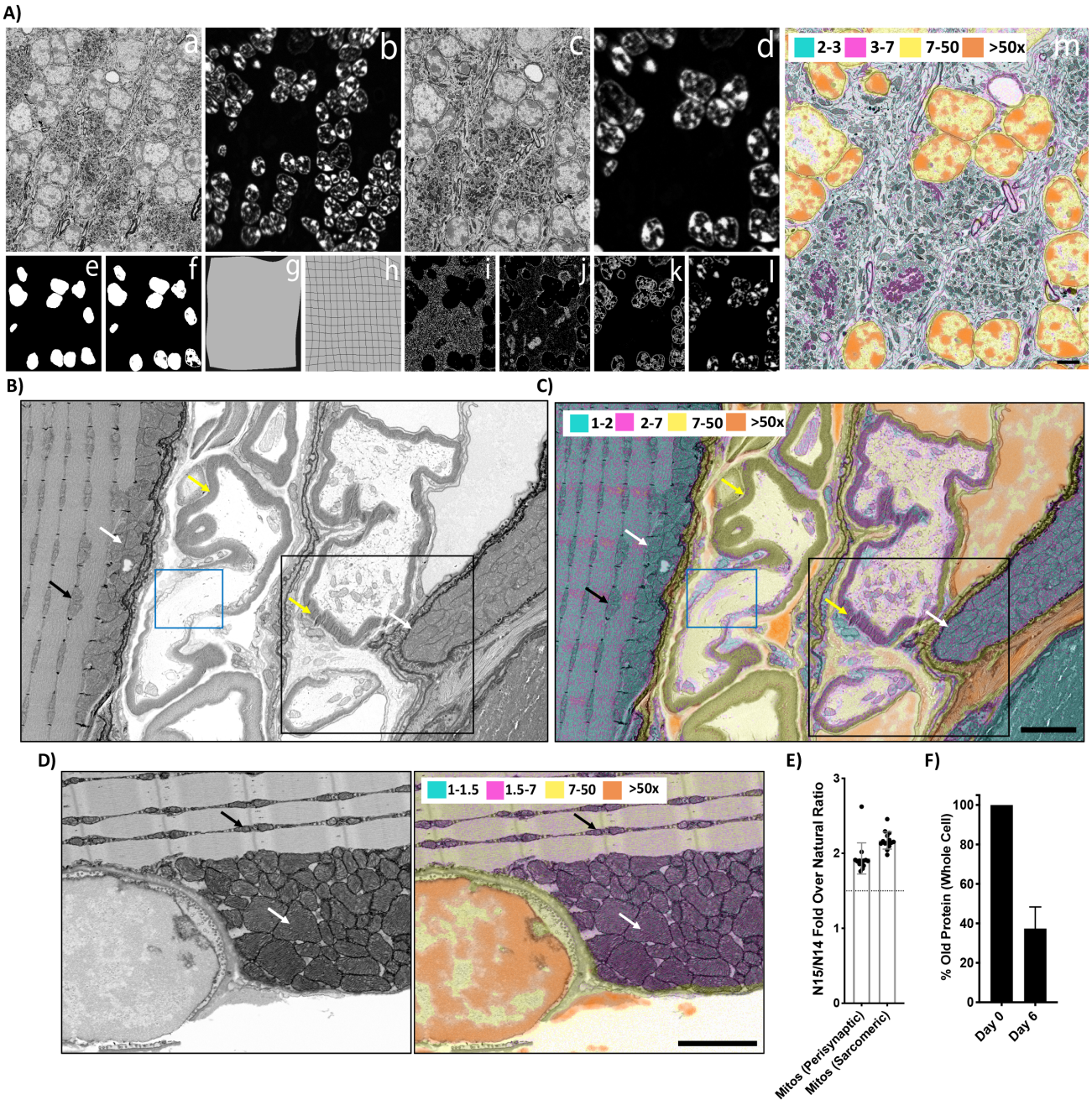

Figure S1. MIMS-EM imaging of cerebellum, neuromuscular junction and intercostal muscles in 6-month old mice, Related to Figure 1.

A) Alignment of SEM and MIMS images using the Mesofusion Plugin (See methods). **a)** SEM and **b)** MIMS uncropped images of cerebellar neurons from a 6-month chase mouse. **c)** SEM and **d)** MIMS images after the ReScale and ReSize tool. **e)** SEM and **f)** MIMS barebones images

after the Create Layout tool. **g-h)** Images containing warping information after the UnwarpJ tool. Categorization of N^{15}/N^{14} ratio signals from **i)** 74-111 x 10^{-4} **j)** 111-259 x 10^{-4} **k)** 259-1850 x 10^{-4} **l)** > 1850 x 10^{-4} using Categorize Ratio Map tool. **m)** Aligned, categorized and colorized final image using the Colorize Ratio Map tool. **B)** SEM and **C)** MIMS overlay of myelinated axons near a neuromuscular junction in intercostal muscle from a 6-month chase mouse. Myelinated axons (yellow arrows) with a Node of Ranvier (blue rectangle) are seen next to a large intercostal muscle fiber with perisynpatic mitochondria aggregates at the edge of the fiber (white arrow, left) and sarcomeric mitochondria in the fiber (black arrow). The inset (black rectangle) containing two myelinated axons with mitochondria (myelin, yellow arrow) and another perisynaptic mitochondria aggregate in the muscle fiber (white arrow, right) is magnified in Figure 1D. $^{15}N/^{14}N$ signal thresholds: 1-2x (cyan), 2-7x (magenta), 7-50x (yellow), >50x (vermillion). **D)** SEM (left image) and MIMS Overlay (right image) of intercostal muscle fiber containing perisynaptic mitochondria aggregates (white arrow) next to a nucleus and sarcomeric mitochondria within the muscle fiber (black arrow). $^{15}N/^{14}N$ signal thresholds: 1-1.5x (cyan), 1.5-7x (magenta), 7-50x (yellow), >50x (vermillion). **E)** Graph shows $^{15}N/^{14}N$ ratio for both perisynaptic and sarcomeric mitochondria (Mitos perisynaptic, n=14, Mitos Sarcomeric, n=14). A dotted line is drawn at the background $^{15}N/^{14}N$ signal of 1.5xNR. **F)** Graph shows %old protein in whole neurons at day 0 (n=5 cells) and day 6 (n=6 cells) as measured by RITE tag turnover in Fig 1H.

For all graphs, error bars indicate standard deviation. Scale bars are 5μm.

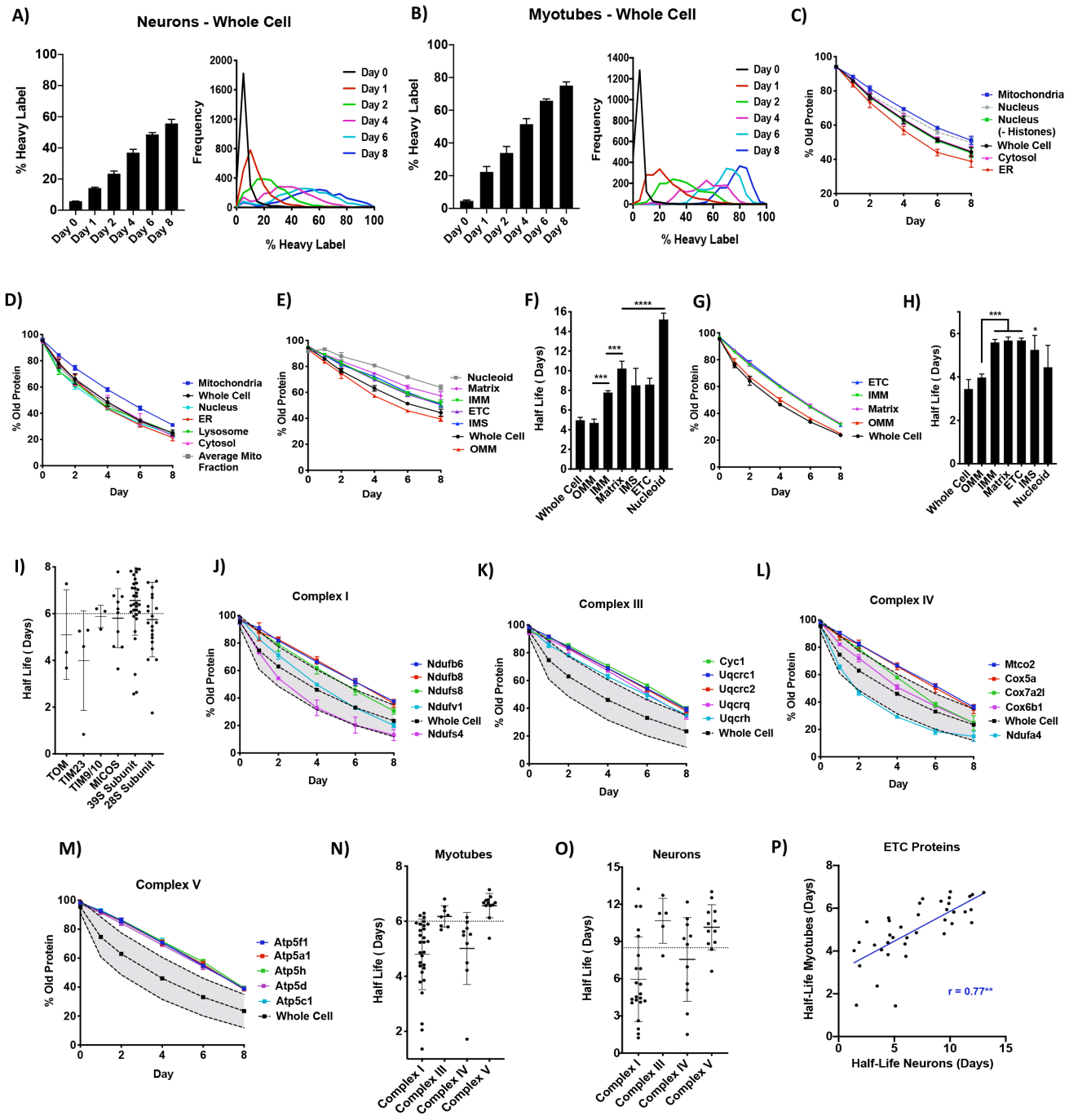

Figure S2. Protein turnover in subcellular organelles and ETC complexes in neurons and myotubes, Related to Figure 2.

A-B) Incorporation of heavy amino acids in the whole cell proteome of **A)** neurons and **B)** myotubes during the SILAC time-course. Graph on left shows %heavy label from day 0-8, and histogram on right shows the frequency of proteins plotted against the %heavy label over the

time-course. **C)** Protein turnover in different subcellular organelles in neurons. Graph shows %old protein for day 0-8 for the Whole Cell, Nucleus, Nucleus (-Histones), Mitochondria, ER and Cytosol. **D)** Protein turnover in different subcellular organelles in myotubes. Graph shows %old protein for day 0-8 for the Whole Cell, Nucleus, Average Mito fraction, Mitochondria, ER, Lysosome and Cytosol. **E-F)** Protein turnover in different mitochondrial subcompartments in neurons. Graph shows **E)** % old protein for day 0-8 and **F)** Half-lives for the Whole Cell, outer mitochondrial membrane (OMM), inner mitochondrial membrane (IMM), Matrix, intermembrane space (IMS), electron transport chain (ETC) and Nucleoid proteins. **G-H)** Protein turnover in different mitochondrial subcompartments in myotubes. Graph shows **G)** %old protein for day 0-8 and **H)** Half-lives for Whole cell, OMM, IMM, Matrix, ETC, IMS and nucleoid proteins **I)** Dot plot representing half-lives of the different proteins in the TOM, TIM23, TIM9/10 and MICOS complexes and the 28S and 39S ribosomal subunits in myotubes. **J)** Protein turnover in the ETC Complex I in myotubes. Graph shows %old protein for day 0-8 for the different CI subunits. **K)** Protein turnover in the ETC Complex III in myotubes. Graph shows %old protein for day 0-8 for the different CIII subunits. **L)** Protein turnover in the CIV in myotubes. Graph shows %old protein for day 0-8 for the different CIV subunits **M)** Protein turnover in the CV in myotubes. Graph shows %old protein for day 0-8 for the different CV subunits. **N-O)** Dot plot representing half-lives of the different proteins in the CI, CIII, CIV and CV in **N)** myotubes and **O)** neurons. **P)** Scatter Plot showing half-lives of ETC proteins in neurons vs myotubes with a spearman correlation coefficient of r=0.77.

For all protein turnover graphs, the average whole cell is the dashed black line and the shaded grey area within dotted lines is the standard deviation for the fraction. For all half-life graphs, error bars indicate standard deviation. For all half-life dot plots, a dotted line is indicated for a half-life of 6 days for myotubes and 8.5 days for neurons, the cut-off used for mitoLLPs. Data are from n=3. *p <0.05, ***p<0.001, ****p<0.0001.

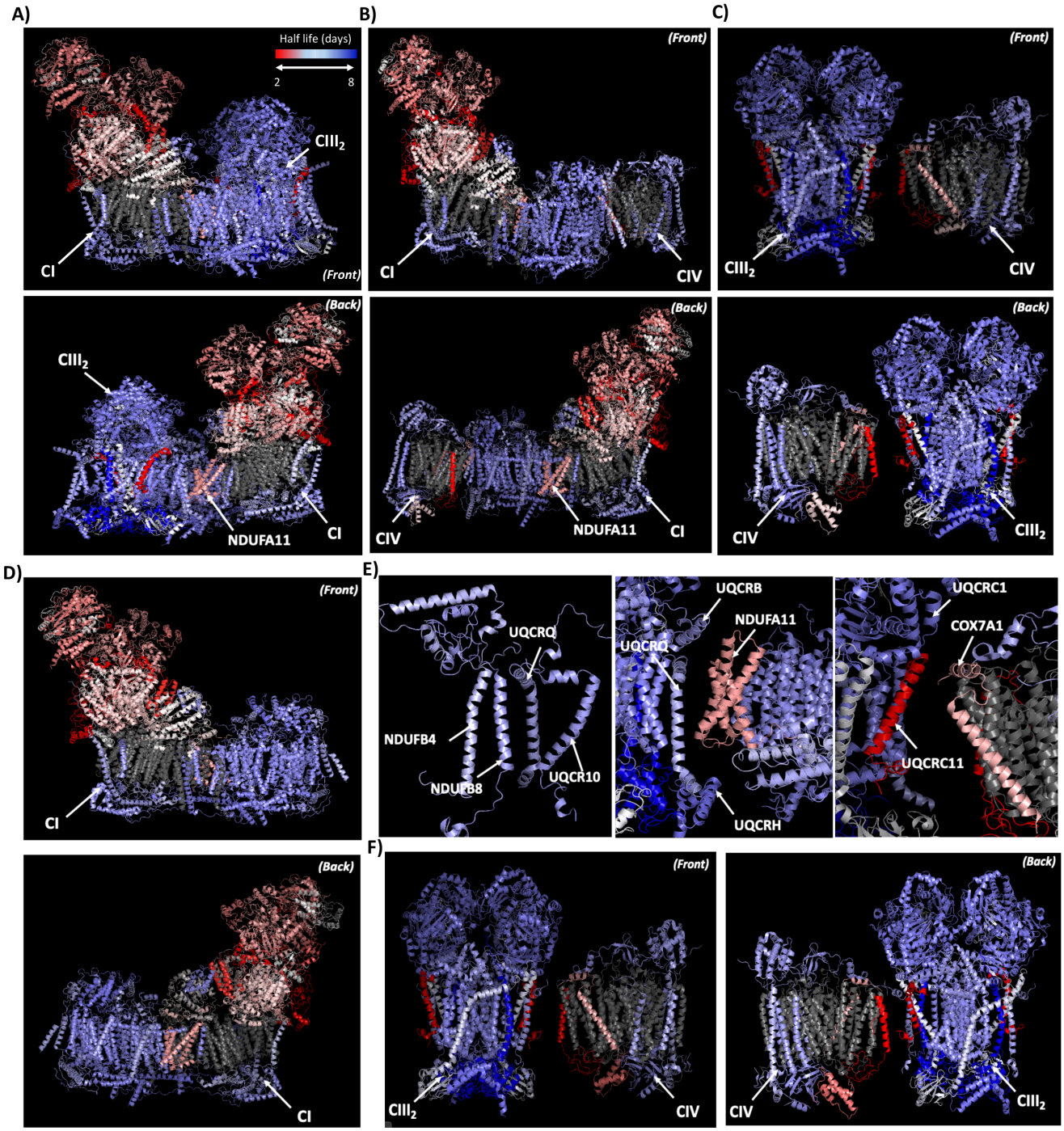

Figure S3. Protein turnover of ETC subunits in respiratory supercomplexes in myotubes, Related to Figure 4.

A,B,C) Turnover of subunits in the respirasome supercomplex with individual complexes removed for clarity. Images show **A)** CI and $CIII_2$ **B)** CI and CIV, **C)** $CIII_2$ and CIV of the porcine respirasome structure from the front (top) and back (bottom). CI, $CIII_2$, CIV and subunit

NDUFA11 are indicated. **D)** Images show turnover of subunits in CI from the porcine respirasome ($CIII_2$ and CIV removed) from the front (top) and back (bottom). **E)** Turnover of contact sites between the different complexes within the porcine respirasome. Contact site between CI and $CIII_2$ containing NDUFB4, NDUFB8 from CI and UQCRQ, UQCR10 from $CIII_2$ (left image), between CI and $CIII_2$ containing UQCRB, UQCRQ, UQCRH from $CIII_2$ and NDUFA11 from CI (middle image) and between $CIII_2$ and CIV containing UQCRC1, UQCRC11 from $CIII_2$ and COX7A1 from CIV (right image). **F)** Image shows turnover of subunits in the intermediate supercomplex using the porcine respirasome structure with CI removed from the front (left) and back (right). $CIII_2$ and CIV are indicated.

The scale of half-lives for all images is 2 to 8 days color-coded from dark red to white to dark blue. The proteins with no coverage in mass spectrometry are colored grey. Data are from an n=3.

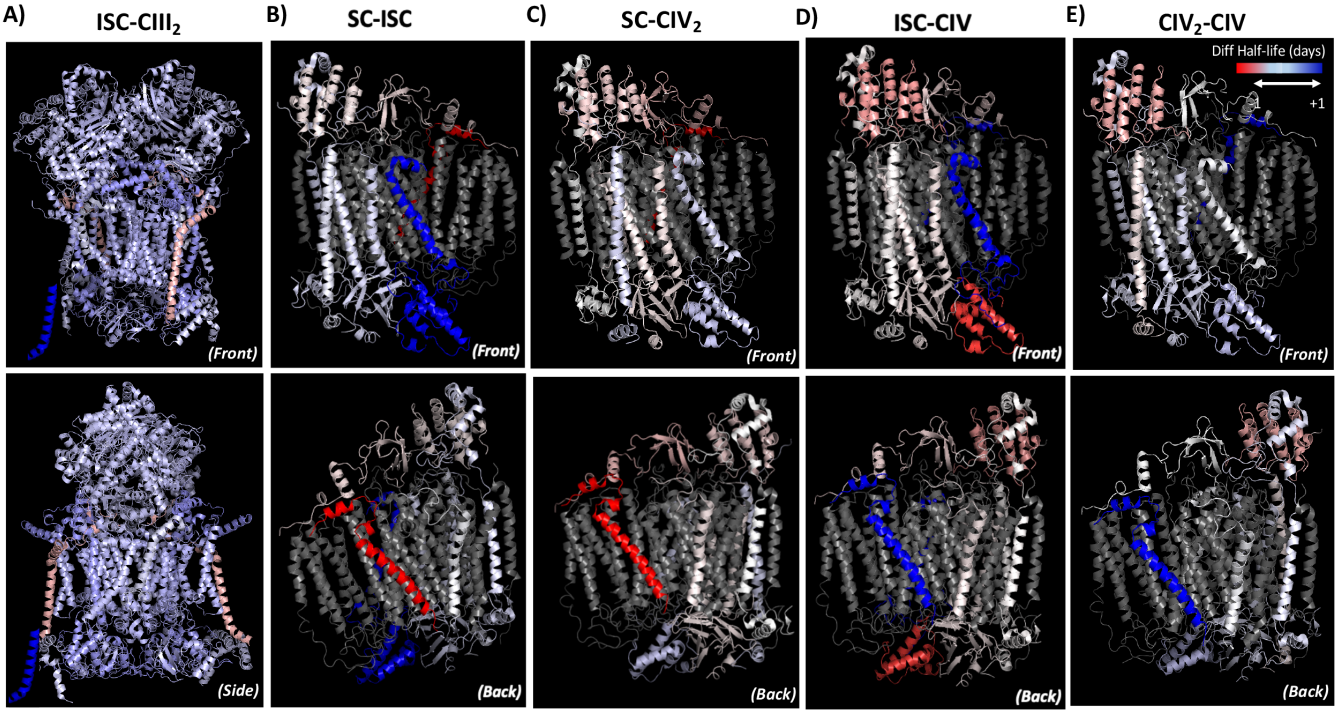

Figure S4. Differential protein turnover of ETC subunits between supercomplexes and individual complexes in myotubes, Related to Figure 4.

Images show differential turnover between **A)** the intermediate supercomplex (ISC) and $CIII_2$, **B)** supercomplexes (SC) and the intermediate supercomplex (ISC) for CIV, **C)** supercomplexes (SC) and CIV_2 (dimer), **D)** intermediate complex (ISC) and CIV (individual complex), **E)** CIV_2 (dimer) and CIV (individual). The top panel represents the front, and the bottom panel represents the side for CIII and back for CIV. The scale for differential turnover structures is in the range of -1 to +1 days from dark red to white to dark blue representing faster turnover in SCs to slower turnover in SCs. The proteins with no coverage in mass spectrometry are colored grey. Data are an n=3.

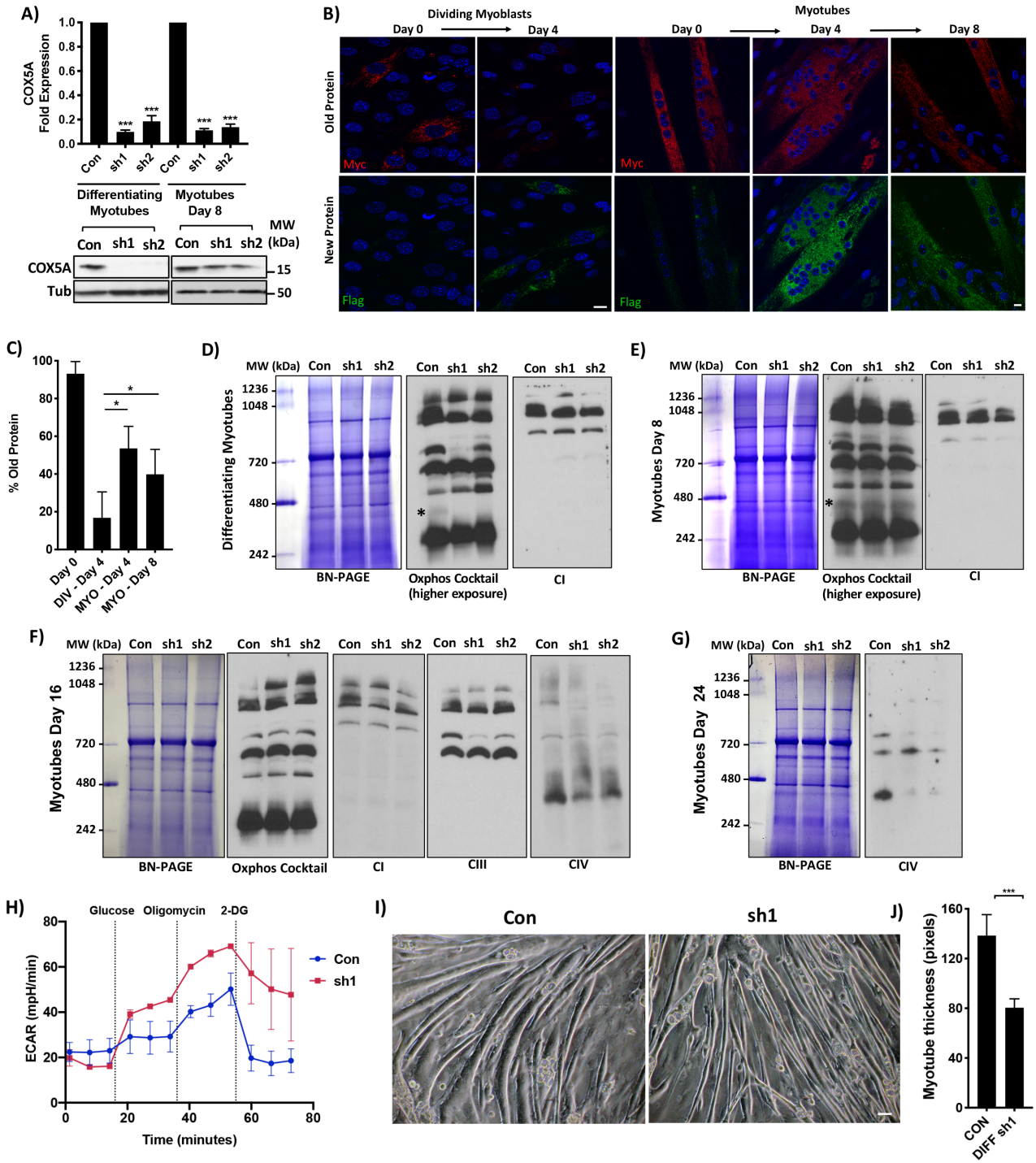

Figure S5. Role of COX7C turnover on ETC complexes, mitochondrial function and myotube size, Related to Figure 5.

A) COX5A mRNA levels (qPCR, top panel) and protein levels (western blot, bottom panels) with control and COX5A-hairpins (sh1, sh2) in differentiating myotubes and fully differentiated

myotubes at day 8. Western blot shows Tubulin as loading control. **B)** Images with lower magnification showing COX7C turnover as measured by RITE. Images show Myc tag (old protein, top panel) and Flag tag (new protein, bottom panel) at day 0 and 4 in dividing myoblasts (left) and day 0, 4 and 8 in myotubes (right). **C)** Graph shows %old protein in dividing myoblasts at day 0 and day 4, and fully differentiated myotubes at day 0, day 4 and day 8 as measured by RITE tag turnover in Fig 5D& S5B. **D-E)** BN-PAGE (left gel) and western blots (right) show levels of all the complexes (Oxphos cocktail, higher exposure) and CI containing complexes in **D)** differentiating myotubes and **E)** Day 8 myotubes in control and COX7C hairpins. Asterisk indicates the individual CIV complex band in the higher exposure of the Oxphos cocktail blot. **F)** BN-PAGE (left gel) and western blots (right) show levels of all the complexes (Oxphos cocktail) and CI, CIII and CIV containing complexes in day 16 myotubes in control and COX7C hairpins. **G)** BN-PAGE (left gel) and western blot (right) show levels CIV containing complexes in day 24 myotubes in control and COX7C hairpins. **H)** Extracellular Acidification Rates (ECAR) in mpH/min over a seahorse assay of 80 minutes and in control and sh1-mediated COX7C knockdowns in differentiating myotubes. Injection timing of Glucose, Oligomycin and 2-DG is indicated with dotted lines. **I-J)** Myotube size with COX7C knockdowns. **I)** Images and **J)** graph show myotube thickness in control and sh-1 mediated knockdowns in differentiating myotubes.

For all graphs, error bars represent standard deviation from an n=3. *$p<0.05$, ***$p<0.001$. Scale bars are 10μm (B) and 50μm (I). Blot markers are indicated.